Evolution of stress-induced thermal anisotropy in granular materials: A directed network perspective

Wenbin Fei [a], Xianze Cui [b], Guillermo A. Narsilio [a,*]

[a] Department of Infrastructure Engineering, The University of Melbourne, Parkville, Australia
[b] College of Hydraulic & Environmental Engineering, China Three Gorges University, Yichang, China.

HIGHLIGHTS

- Stress variation does not always synchronize with thermal conductivity evolution.
- However, thermal conductivity reaches a common terminal value at large strain.
- Interparticle contacts orientation contributes to high thermal conductivity.
- New *directed network thermal resistance R* considers three contact attributes.
- R is inversely proportional to anisotropic thermal conductivity.

GRAPHICAL ABSTRACT
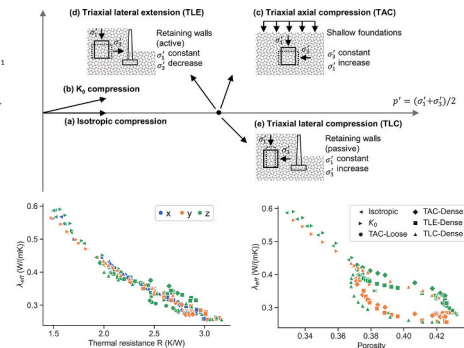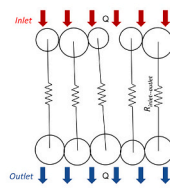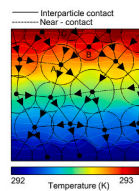
ARTICLE INFO

ABSTRACT

External stress can induce anisotropic effective thermal conductivity λ_{eff} in granular assemblies. However, few studies have used a proper microstructural parameter to study the evolution of thermal anisotropy. In this paper, deformed particle assemblies under different stress paths were generated using discrete element method. By considering each particle as a node, and each heat transfer path via interparticle contact or particle-air-particle as a directed edge, a novel directed thermal network was constructed and a sample-scale parameter named *"directed network thermal resistance R"* was introduced. Results show contact attributes (i.e., connectivity, quality and orientation) not only dominate the value but also the evolution of anisotropic λ_{eff} that calculated using thermal network models. R has the merit of considering the three contact attributes and shows a general inverse linear relationship to anisotropic λ_{eff} regardless of the dominant heat transfer direction, and its ratio can capture the evolution of thermal anisotropy.

1. Introduction

Effective thermal conductivity (λ_{eff}) quantifies the heat transfer capacity, playing a vital role in engineering applications such as geothermal engineering [1], oil and gas extraction [2], dam engineering [3] and carbon dioxide geological storage [4]. Geostatic stress changes
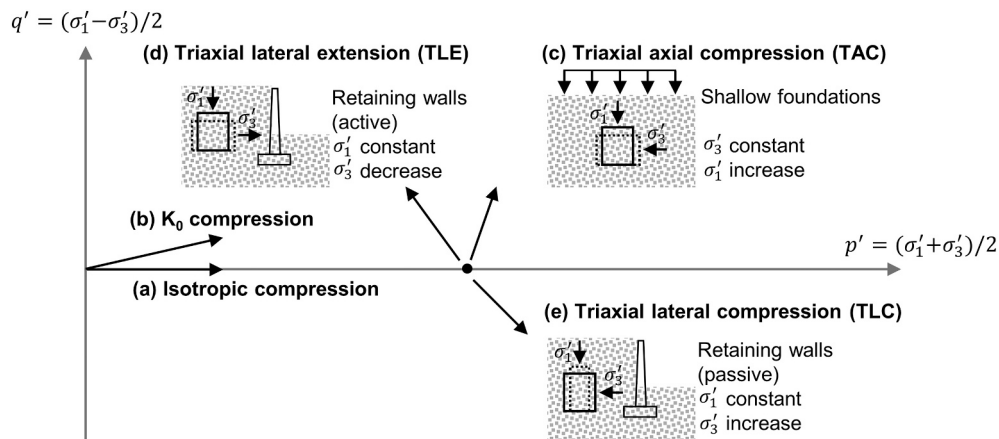

Fig. 1. Stress paths for numerical experiments using DEM.

during the construction or operation of these applications and may induce anisotropic λ_{eff} when heat transfer is measured in different directions. For example, an energy pile is a dual-function structure that can bear building loads and exchange heat with the ground [5]. The soils surrounding the energy pile will be squeezed and sheared during pile driving, resulting in localised stress anisotropy which can lead to thermal anisotropy. Therefore, it is of great importance to study stress-induced thermal anisotropy in granular materials.

It is known that λ_{eff} of a granular material is controlled by its internal microstructure (e.g., porosity, particle shape, particle connectivity, and particle size distribution) and external environmental conditions such as temperature and applied stress [6–8]. External stress will make the particles rearrange, so the particle contact condition and heat transfer paths change [9]. However, the importance of stress to the variation of microstructure and the evolution of anisotropic λ_{eff} lack sufficient attention. Few microstructural parameters can be used to build models for predicting the degree of anisotropy in λ_{eff}.

Most of the existing models only consider porosity as the sole structural parameter [10]. Another type of model considers packing structure using Voronoi polyhedral [11], rotational symmetry of particles [12], typical lattice structures [13] and mean local curvature and minimum gap between particles [12,14]. Pressure-dependent models have been introduced incorporating loading direction stress, Young's modulus and packing arrangement coefficient [15–17]. However, these models can only predict λ_{eff} in the same direction as the porosity, structural characterisation and loading direction stress cannot reveal the directional property of the microstructure in granular materials. Zhao et al. (2020) [18] also recognised that most of existing models focus on the thermal conductivity in a specified direction, and they constructed a thermal conductivity tensor for non-spherical particles. An attempt by Garrett and Ban [19] estimated anisotropic λ_{eff} based on thermal conductivity of different constituents and vertical/horizontal stress ratio (i. e., Jaky's at-rest earth pressure coefficient in the field of soil mechanics). Nevertheless, this approach may not be suitable to predict stress-induced anisotropic λ_{eff} since the vertical/horizontal stress ratio varies.

The implementation of network analyses to granular materials has enriched the mesoscale structural parameters available for the analysis of mechanical, hydraulic and thermal behaviours [20–22]. A network is a web in which nodes are connected by edges. The definitions of nodes and edges vary for different network types. In a *contact* network, prompt to indicate mechanical failure according to the examination of particle arrangement structural evolution, a node represents a particle while an edge represents an interparticle contact. It is known that heat not only transfers through interparticle contacts but also via particle-void-particle when two neighbouring particles are nearly in contact. Hence, more edges are generated to represent these near-contacts, extending a contact network to a *thermal* network. Extensive research about the

relationship between thermal network features and λ_{eff} in sphere packings and real irregular sands have been studied in our previous work [23,24]. However, the network features were computed from undirected thermal networks in which the heat transfer direction between two particles was ignored (i.e., the network edge was undirected). Generally, undirected graphs only represent whether or not a connection exists between two nodes. In contrast, if a node *a* in a directed graph is connected to node *b,* it does not necessarily mean that node *b* is also connected to node *a.*

Heat always moves from a particle with high temperature to a particle with low temperature, so the pre-assigned temperature boundary condition determines the dominant heat transfer direction between particles, i.e., along the thermal network edges. It has been known that contact number and interparticle contact area affect heat transfer and they evolve with the increase of external loadings. However, contact orientation, as another characteristic of contact, is usually ignored when developing λ_{eff} models. It has been found that intensifying the contacts along the heat transfer direction is an economical method to improve the λ_{eff} [25,26]. Mohamad [27] revealed that aligning a small number of long particles with the prescribed temperature gradient can lead to a 30% increase of λ_{eff}. Therefore, it is necessary to identify a microstructural parameter that can include particle connectivity, contact quality and contact orientation simultaneously.

The application of complex network theory to directed networks has the inherent advantage to deal with this issue since (1) it can characterise particle connectivity to address the rarity of mesoscale structural parameters in soil characterisation. Compared with the widely used coordination number that only quantifies the local neighbourhood of a particle, the variety of network features can cover a longer distance from one end of a soil sample to the opposite end. This unique end-to-end property makes the network features good candidates for studying the force-transmission and heat transfer paths through a sample. (2) In networks, an edge can be assigned a weight to indicate the capacity of mass transfer. Hence, parameters from a weighted network can indicate the contact quality or heat transfer capacity. (3) In sphere packings, the edge linking two neighbouring particles passes through the centre of the contact perpendicularly, so the edge orientation is the contact orientation.

Inspired by the merits of complex network theory introduced by Tordesillas et al. in mechanics [28,29], this work built directed networks for granular materials and then generate a directed thermal resistance R as the mesoscale microstructural parameter sought after. Several numerical experiments including isotropic compression, K_0 compression (zero lateral deformation), and triaxial tests were conducted using the discrete element method (DEM). The evolutions of particle connectivity, contact quality, contact orientation and R due to the stress-induced sample deformation, as well as their relationship to variation of

Table 1
Details of key parameters used in the DEM simulations.

Parameters	Values
Density (kg/m^3)	2600
Young's modulus (GPa)	1
Poisson's ratio	0.2
Sphere radius (mm)	0.3–0.35
Friction coefficient	Refer to the specific experiment
Rolling friction coefficient	Refer to the specific experiment
Particle-wall friction condition	Smooth
Stiffness of boundary walls	Rigid
Time step (s)	1e-7
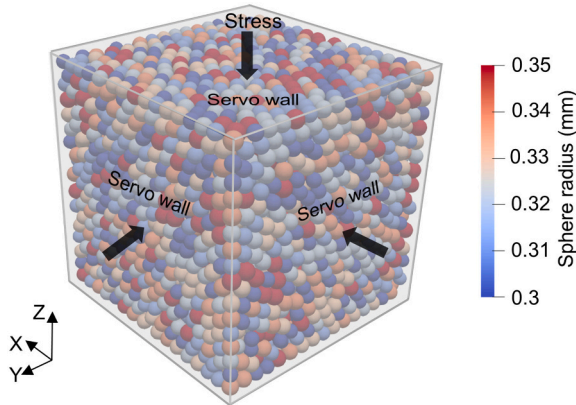
Fig. 2. DEM simulation of isotropic compression.

anisotropic λ_{eff} were investigated.

2. Discrete element numerical experiments

Over the last decade, geotechnical engineering has growing interest in a new field of energy geotechnics [30,31], including shallow and deep geothermal systems. Shallow foundations can serve as an energy source or sink for geothermal engineering [32]. Dual functional structures such as energy piles, energy tunnels and energy retaining walls were also developed to provide both mechanical support for their above buildings and heat energy exchanging with the ground [5,32]. In these different applications, soil can experience distinct stress-strain history (Fig. 1) following different stress paths, typically (1) axial compression for shallow foundations; (2) lateral extraction for active earth pressure behind a retaining wall; and (3) lateral compression for passive earth pressure behind a retaining wall.

Discrete element methods (DEM) have been used in this work to simulate these cases through numerical triaxial tests in which stress anisotropy and soil failures were induced by shear stresses. Zero lateral strain (K_0) compression test was also simulated to investigate the anisotropy caused by compressive stress and compared against another isotropic compression experiment (i.e., a base case). Both loose sand and dense sand were used in triaxial tests to investigate the effect of contraction and dilation on their microstructure and anisotropic λ_{eff}. In summary, six numerical experiments were conducted, including:

- Isotropic compression
- K_0 compression
- Triaxial axial compression (TAC) for loose sand
- Triaxial axial compression for dense sand
- Triaxial lateral extension (TLE) for dense sand
- Triaxial lateral compression (TLC) for dense sand

2.1. Sample generation

In this work, an open-source discrete element software LIGGGHTS [33] was utilised for three-dimensional (3D) sample generation. >5000 spheres were included in each granular assembly generated in DEM to achieve a representative sample size for its macroscopic behaviour analysis [34,35]. The spheres were initially dispersed in a relatively large box, a homogeneous sample with the target porosity was achieved by moving the rigid walls of the box. Hertz-Mindlin contact law was employed to simulate stress-dependent behaviours. Table 1 summarises the parameters used in DEM numerical experiments. The stresses on the sample boundaries were controlled by a servo-controlled feedback system. To maintain the computational stability when integrating the motion equations in DEM, the timestep and strain rate in the direction of loading in DEM simulation were selected to keep the inertial number I (Eq. (1)) smaller than 2.5e-3 [36,37]:

$$I = \dot{\varepsilon} d \sqrt{\frac{\rho}{p'}} \tag{1}$$

where $\dot{\varepsilon}$ is the strain rate, d is the mean particle size, ρ is the particle density, and p' is the mean effective stress.

2.2. Isotropic compression

An initial sample was first prepared by allocating 5968 spheres in a relatively large box with an edge size of 15 mm, followed by moving all walls of the box with the same velocity until the porosity reached 0.4. Next, stress was applied to each wall to reach 1500 kPa in nine steps, as shown in Fig. 2. No friction was included during the DEM simulation to ensure the sample is homogeneous so it can be used as a reference to compare with other experiments.

2.3. K_0 loading

The same initial sample with the porosity of 0.4 used for isotropic compression was compressed following a zero lateral strain K_0 loading condition in which the vertical stresses were always 1.2 times as much as the horizontal stresses. All the stresses were increased in nine steps until the vertical stress reached 1500 kPa. The evolution of particle arrangement under the K_0 loading condition resulted in a distinct soil fabric from that in the isotropic compression numerical experiment. In this case, heat transfers along vertical and horizontal directions were estimated and hypothesised to be different due to the stress-induced anisotropy.

2.4. Triaxial axial compression (TAC)

To investigate the stress-induced thermal anisotropy in shallow geothermal foundations, triaxial axial compressions were simulated for both loose sand and dense sand in three stages: (1) sample preparation, (2) consolidation and (3) loading. Similar to the sample preparation for isotropic compression, 9549 spheres were distributed in a box with a height of 30 mm, and width and length of 15 mm. Since the height at the vertical direction was twice the length in horizontal directions, the top and bottom walls of the box were moved at a velocity that is twice as fast as the velocity in horizontal directions. The porosity was monitored when moving the walls until the porosity reached 0.432 for a loose sand sample. Next, a confining pressure of 100 kPa was applied on each wall to enable the sample to experience a "consolidation" process. During the sample preparation and consolidation, the sliding and rolling friction coefficients were set as 0.95 and 0.1, later changed to 0.5 and 0 in the loading stage. In the loading stage, while maintaining the pressure on the horizontal walls as 100 kPa, the top and bottom walls were moved vertically at a velocity of 0.005 m/s corresponding to an inertial number I of 1.31×10^{-5} to achieve a quasi-static condition. The experiment was
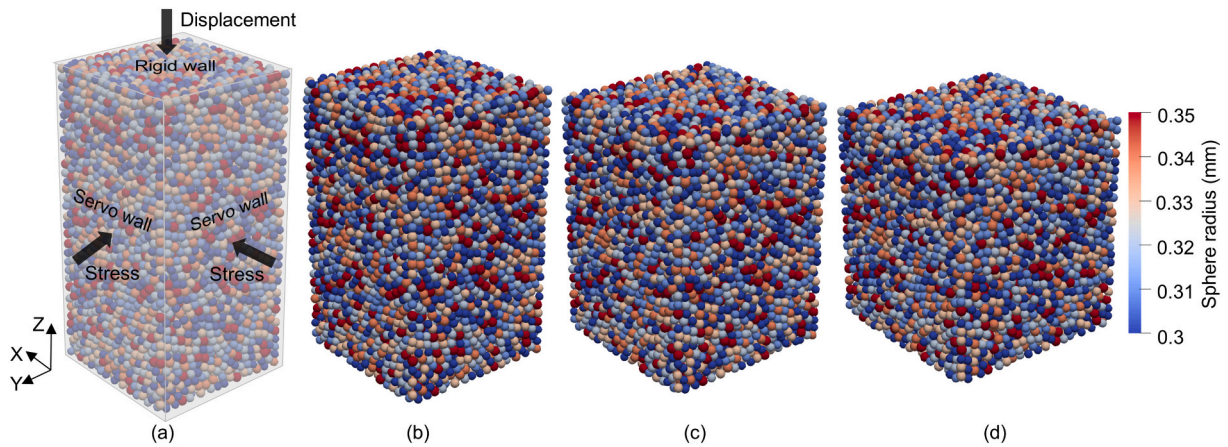
Fig. 3. DEM simulation of triaxial axial compression of a dense sand after consolidation (a), axial strain reached 10% (b), 20% (c) and 30% (d).
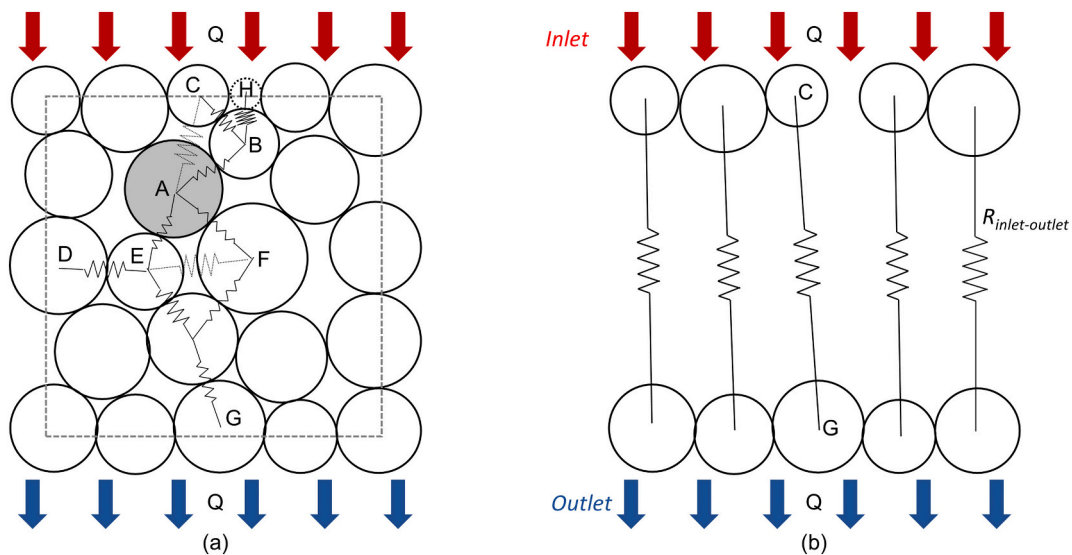

Fig. 4. Thermal resistors are used to represent the heat transfer between neighbouring particles (a). If they are in the preferential heat transfer path, they are connected in series and represented as a long inlet-outlet resistor $R_{inlet-outlet}$ (b). The resistors in (a) shown with the solid line are related to interparticle contacts while dash lines correspond to the particle-air-particle heat paths.

stopped when the vertical axial strain reached 30%, this is a very large strain to be able to capture and compare any potential softening/peaks/dilation effects for the dense samples.

Triaxial axial compression experiment for dense sand was simulated using a similar three stages except that the sliding and rolling friction coefficients were 0.5 and 0 in all the stages. The sample deformations with vertical axial strain at 0 (after consolidation) to 10%, 20% and 30% are shown in Fig. 3. With the top and bottom walls moving close to each other, the side walls moved away from their pairs. The side walls in this work were rigid, which was different from the soft membrane used in the laboratory experiment.

2.5. Triaxial lateral extension (TLE)

The dense sample after the consolidation for the TAC test was also used for triaxial lateral extension. Instead of moving the top and bottom walls, the two pairs of horizontal walls in x and y directions were moved far from each other while keeping the pressure on the top and bottom walls as 100 kPa during the loading stage.

2.6. Triaxial lateral compression (TLC)

The "consolidated" dense sand sample from TAC was also used for triaxial lateral compression. Instead of compressing the sample in the long axial direction by moving the top and bottom walls, at the loading stage of triaxial lateral compression, the pairs of side walls were moved close to each other while maintaining 100 kPa pressure on top and bottom walls.

3. Directed thermal network

3.1. Directed network thermal resistance

In dry granular materials, heat moves mainly through interparticle contacts (A-B in Fig. 4(a)) followed by particle-void-particle (A-C in Fig. 4(a)) at a temperature lower than 1000 K [38], which corresponds to the topology of the particle assembly (i.e., particle connectivity). In addition, the interparticle contact area plays a crucial role in heat transfer since it indicates the contact quality and the local heat transfer capacity [39]. In this work, thermal resistors were used to characterise the heat transfer capacity for local heat transfer paths through both interparticle contacts and particle-air-particle consistently. The local
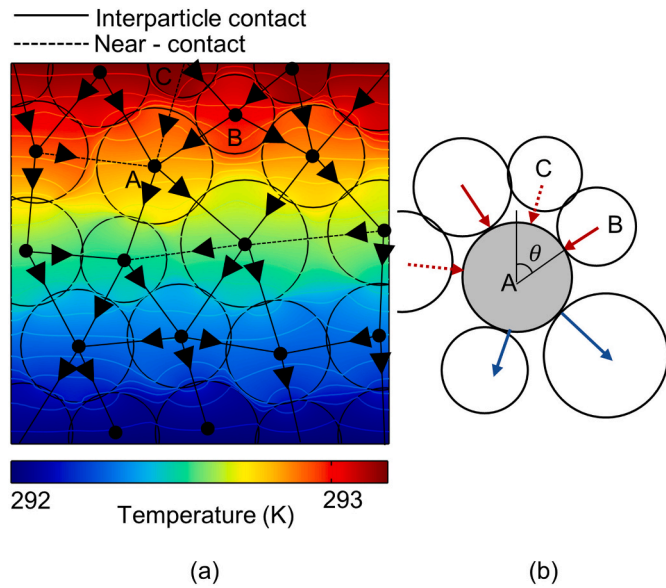
Fig. 5. Temperature distribution in a particle assembly simulated using finite element method and schematic illustration of constructing a directed thermal network (a), and local heat transfer in the neighbourhood of a particle (b).

thermal resistors in the preferential heat transfer path linking two particles at the "inlet" (highest temperature boundary) and "outlet" (lowest temperature boundary) of a sample could be connected in series to form a long inlet-outlet resistor. If the number of particles on the top and bottom boundary is not equal, the unmapped boundary particle results in an extra heat transfer path connecting to another inlet-outlet resistor. For example, potential particle H leads to an extra path H-B in Fig. 4(a). The resistance of the extra local heat transfer path H-B will be added to the resistance of its nearest connected inlet-outlet resistor C-B-A-*E*-G.

After identifying the inlet-outlet resistors for all paired particles along the prescribed temperature gradient direction as shown in Fig. 4 (b), a sample-scale thermal resistance R can be computed using the resistances of these parallel inlet-outlet resistors:

$$R = \left(\sum \frac{1}{R_{inlet-outlet}} \right)^{-1} \quad (2)$$

The thermal network, consisting of nodes and edges, is one of the best tools to abstract the topology of granular materials. The edges in the thermal network can be weighted using thermal resistance, so the resulting network features can indicate both particle connectivity and the connection quality simultaneously [40]. However, the heat flux through an edge is not only related to the thermal resistance but also the temperature gradient as shown in Eq. (3). As a result, although a near-contact resistor such as C-A in Fig. 4 (a) has a larger thermal resistance than an interparticle contact resistor such as D-E, a high vertical temperature gradient in Fig. 4 might lead to more heat transfer via the near-contact than that via the interparticle contact.

$$Q_{ij} = \frac{1}{R_{ij}} \left(T_i - T_j \right) \quad (3)$$

where Q_{ij} is the heat flux and R_{ij} is the thermal resistance between nodes i and j with temperatures T_i and T_j, respectively. Since this paper aims to create a structural parameter to study stress-induced thermal anisotropy, the geometrical information is assumed to be used to indicate the temperature gradient, i.e., particles closer to the higher temperature boundary (called "inlet" herein) are assumed to be warmer than particles closer to the lower temperature boundary (called "outlet").

In this work, the contact orientation was used to indicate the local heat transfer direction after analysing the temperature distribution pattern (Fig. 5) computed using the finite element package COMSOL Multiphysics [41]. The top (inlet) and bottom (outlet) boundary temperatures of the sample were 293.15 and 292.15 K to prescribe a vertical temperature gradient, while the side boundaries were insulated. The thermal conductivities of solid and air were set as 3 W/(m K) [42,43] and 0.025 W/(m K) [44], respectively. It can be observed from Fig. 5 (a) that heat flux between two connected particles is concentrated around the small contact area, and the local temperature gradient between two particles either in contact (B-A) or near-contact (C-A) is almost in the same direction as the network edge. Since the particles are spherical, the contact orientation and local heat transfer direction can be easily determined using particle coordinates. As a result, directed edges and a corresponding directed thermal network could be constructed. The application of directed network edges has the merit of reducing the
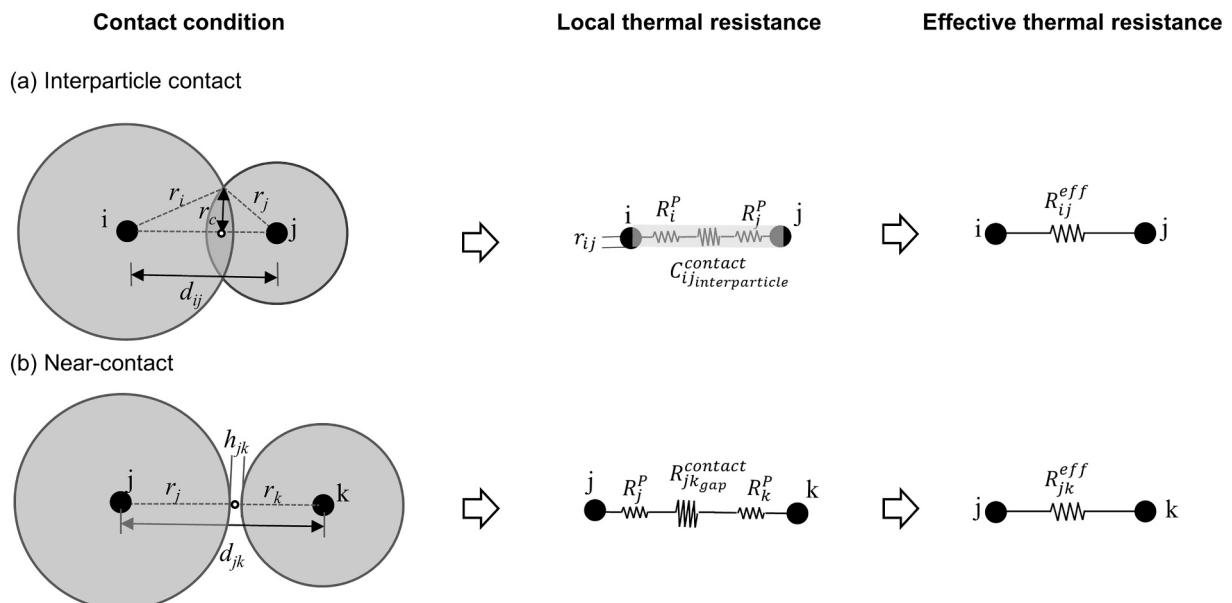

Fig. 6. Thermal resistance computation of a resistor at an interparticle contact (a) and at a near-contact (b).
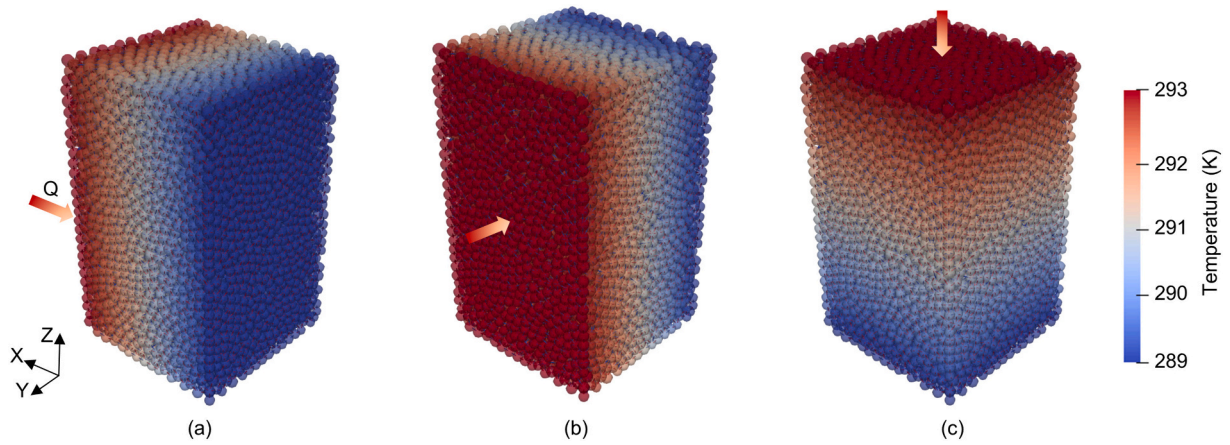
Fig. 7. Heat transfer simulation of the dense sample at the strain of 10% in triaxial axial compression (TAC) tests using thermal conductance network model along with x (a), y (b) and z (c) directions. (For interpretation of the references to colour in this figure legend, the reader is referred to the web version of this article.)
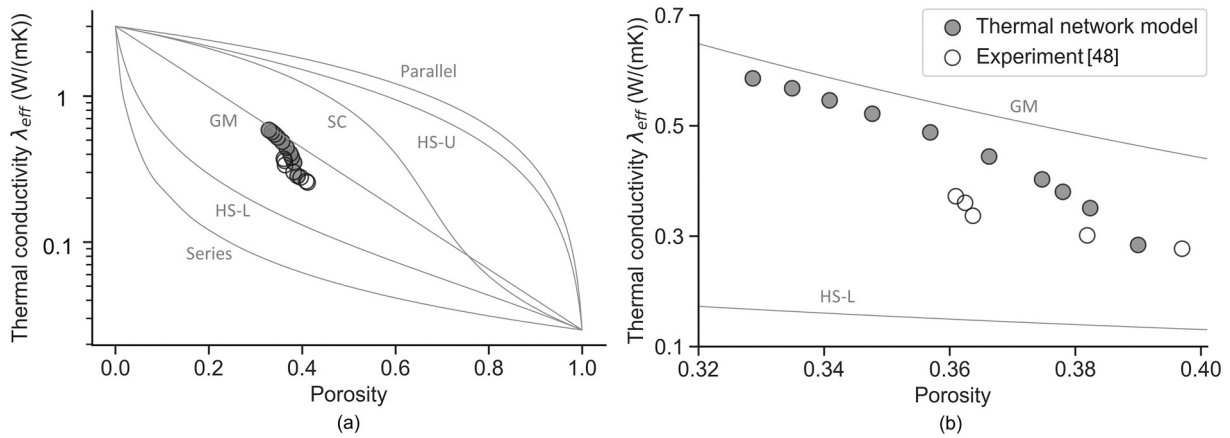

Fig. 8. λ_{eff} calculated using thermal network model(solid circles) compared with experimental (hollow circles) and theoretical (grey lines)results. (a) The whole range of theoretical values. (b) is a subplot of (a).

Table 2
Theoretical λ_{eff} models.

Model	Equation
Series [49]	$\lambda_{eff} = \left(\sum_{i=1}^{N} \frac{f_i}{\lambda_i} \right)^{-1}$
Parallel [49]	$\lambda_{eff} = \sum_{i=1}^{N} f_i \cdot \lambda_i$
Geometric mean (GM) [50]	$\lambda_{eff} = \prod_{i=1}^{N} \lambda_i^{f_i}$
Hashin-Shtrikaman (HS-U: upper bound, HS-L: lower bound) [51]	$\lambda_{eff} = \lambda_1 \left[1 + \frac{3f_2(\lambda_2 - \lambda_1)}{3\lambda_1 + f_1(\lambda_2 - \lambda_1)} \right]$ (Upper: 1 = solid, 2 = air; lower: 1 = air, 2 = solid)
Self-consistent (SC) [52,53]	$\lambda_{eff} = \frac{1}{3} \left[\frac{1-n}{2\lambda_{eff} + \lambda_s} + \frac{n}{2\lambda_{eff} + \lambda_s} \right]^{-1}$

Where λ_i and f_i are the thermal conductivity and the volume fraction of the related phase, n is porosity.

iterations for searching preferential heat transfer paths, so enhancing the speed of identifying the long inlet-outlet resistors in Fig. 4(b). Since contact orientation affects the magnitude of the local temperature gradient and the related local heat flux, for a resistor such as $A \rightarrow B$ with a thermal resistance of $R_{A \rightarrow B}$, only its component $R_{A \rightarrow B}^{eff} = R_{A \rightarrow B} \times cos\theta$ projected on the prescribed boundary temperature gradient direction (from top to bottom in Figs. 4 and 5) is considered as the effective thermal resistance of the resistor.

In Fig. 5 (b), several particles provide the heat sources for particle A but only one path is included in the inlet-outlet resistor. Therefore, the resistances of resistors linking all heat sources were combined to generate an effective local thermal resistance using Eq. (4).

$$R_{ij}^{eff'} = \left(\sum_{n=i}^{N} \left(R_{n \rightarrow j}^{eff} \right)^{-1} \right)^{-1} \tag{4}$$
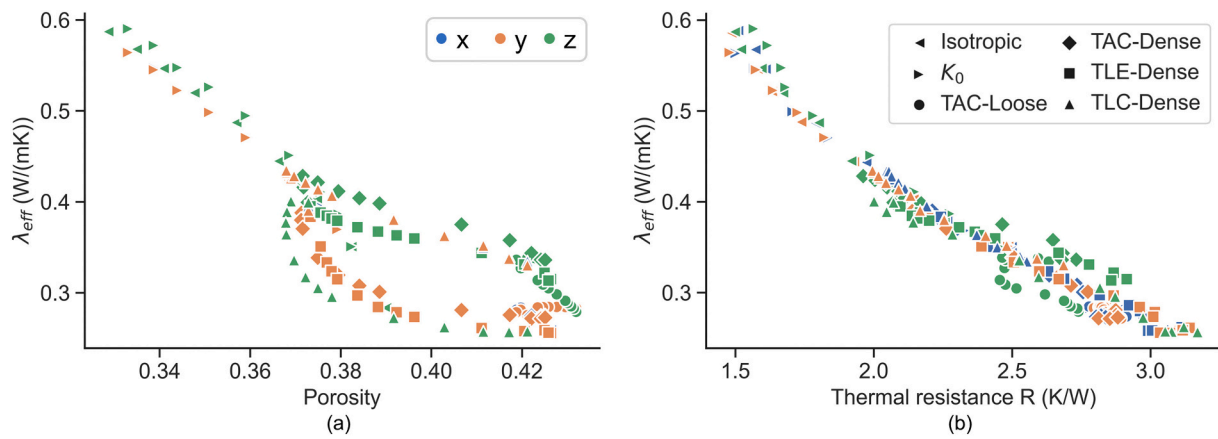
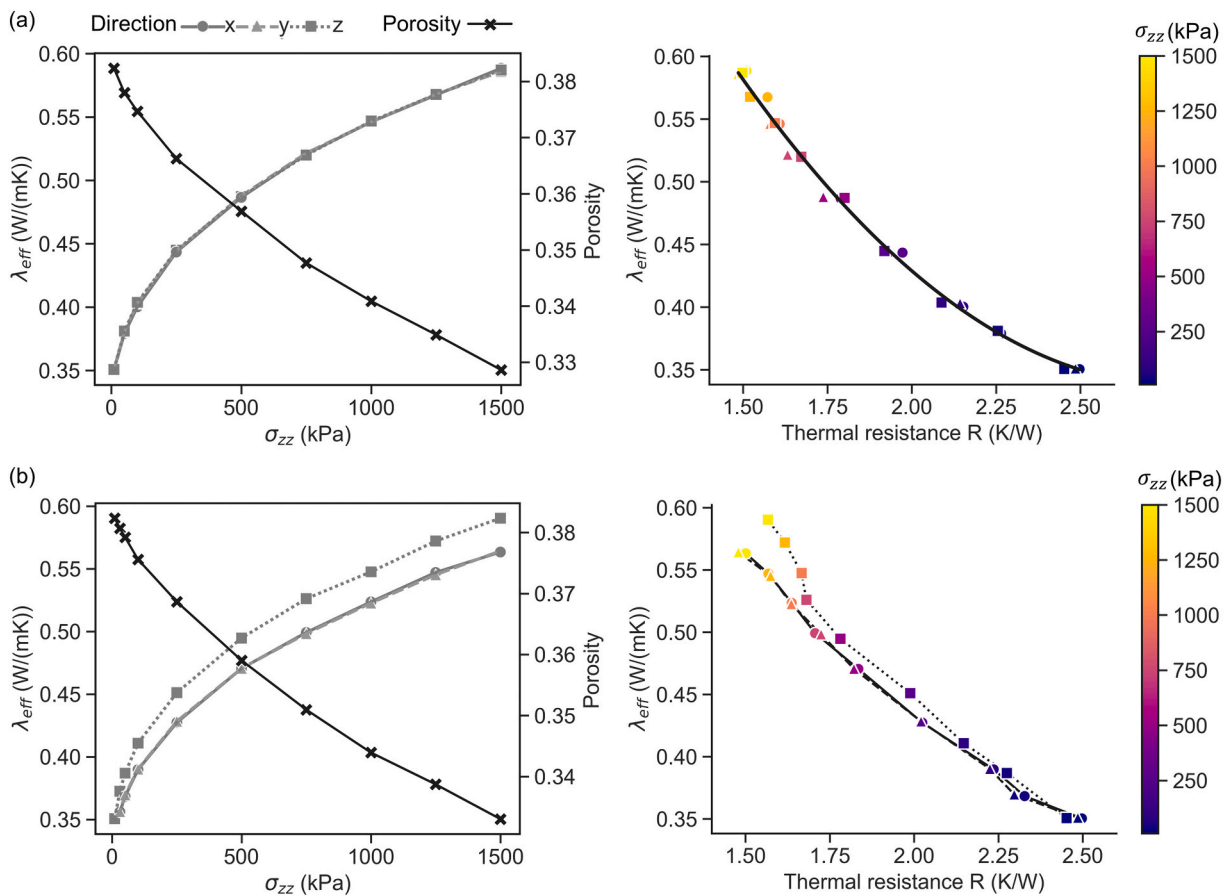**Fig. 9.** Directed network thermal resistance R versus λ_{eff} in various numerical experiments.

Fig. 10. The evolution of λ_{eff} along x, y and z directions and their relationships with directed network resistance R. (a) isotropic compression. (b) K0 compression.

where N is an in-node set. For example, to compute the $R_{AE}^{eff'}$ in Fig. 4 (a), N is a node-set (A, D, F) since all the three nodes are the heat sources of particle E.

3.2. Thermal resistance calculation

The previous section has explained how to compute the sample-scale directed thermal resistance R that is derived from a combination of the thermal resistance of local resistors connecting two neighbouring particles either through interparticle contact or near-contact. This section will introduce the computation of the thermal resistance of the local resistors.

3.2.1. Thermal resistance between two particles in contact

Two spherical particles with an overlapped area can be used to represent the particles in contact, as shown in Fig. 6 (a). This simplification is also widely adopted in DEM software for either stress analysis or heat transfer analysis [45,46]. By considering neighbouring particles (i and j) and the interparticle contact as three resistors, the effective thermal resistance between the two particles is the sum of their thermal resistances since they are connected in series (Eq. (5)).

$$R_{ij}^{eff} = R_i^P + R_{ij_{interparticle}}^{contact} + R_j^P \tag{5}$$

where R_i^P, $R_{ij_{interparticle}}^{contact}$ and R_j^P are thermal resistances of particle i,
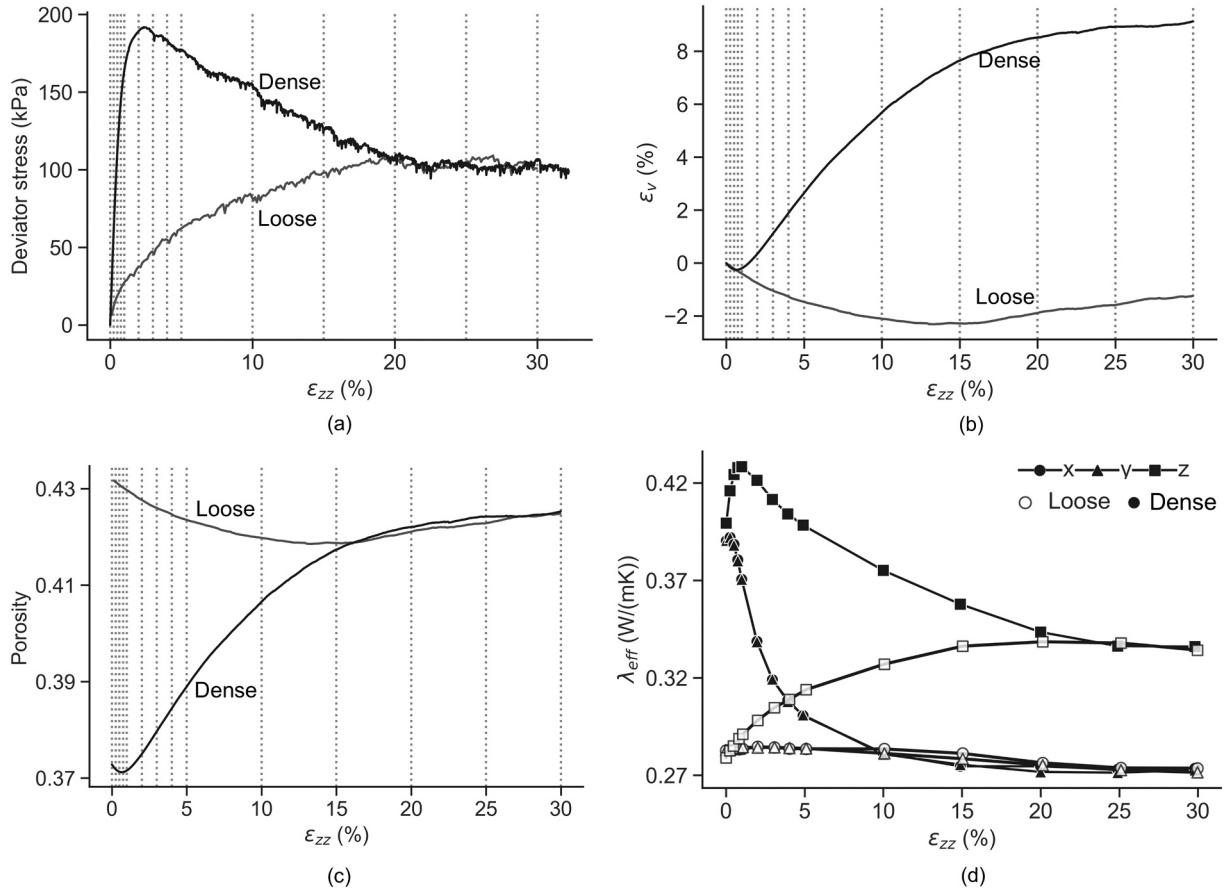
Fig. 11. The evolution of stress (a), volume strain (b), porosity (c) and λ_{eff} (d) in triaxial axial compression tests. The dash lines indicate the axial deformation of 0.25%, 0.5%, 0.75%, 1%, 2%, 3%, 4%, 5%, 10%, 15%, 20%, 25% and 30%.

interparticle contact and particle j, respectively. According to the theoretical study by Batchelor and O'brien [14], the thermal resistance within a particle can be expressed as:

$$R_n^P = \frac{r_n}{\pi \lambda_s \left(r_{ij}^c\right)^2}, n \in [i,j] \tag{6}$$

where r_n is the particle radius, λ_s is the particle thermal conductivity. Considering an equivalent cylinder connecting the two particles and passing through the contact area, its effective radius r_{ij}^c can be defined as Eq. (7) that includes a fraction coefficient χ indicating the curvatures of the spherical particles.

$$r_{ij}^c = \chi \cdot r_{ij} = \chi \frac{2 r_i r_j}{r_i + r_j} \tag{7}$$

where r_{ij} is the radius of the equivalent cylinder, r_i and r_j are the radii of particles i and j. In this work, χ was set as 0.5 following the paper by Yun and Evans [42].

The thermal resistance of an interparticle contact was computed as:

$$R_{ij_{interparticle}}^{contact} = \left(\pi \cdot \lambda_v \cdot r_{ij} \cdot \left[\lambda_c + \Delta \lambda_g + ln\left(\alpha^2\right)\right]\right)^{-1} \tag{8}$$

where λ_v is the air thermal conductivity and λ_c and $\Delta \lambda_g$ were approximate by Batchelor and O'brien [14] as:

$$\begin{cases} \lambda_c = \frac{2 \beta_{ij}}{\pi} \text{ and } \Delta \lambda_g = -2ln\left(\beta_{ij}\right) \text{ if } \beta_{ij} \to \infty \\ \lambda_c = 0.22 \beta_{ij}^2 \text{ and } \Delta \lambda_g = -0.05 \beta_{ij}^2 \text{ if } \beta_{ij} < 1 \end{cases} \tag{9}$$

where β_{ij} is a particle overlap parameter:

$$\beta_{ij} = \frac{\lambda_s}{\lambda_v} \frac{r_c}{r_{ij}} \tag{10}$$

where r_c is the radius of the contact surface as shown in Fig. 6 (a).

3.2.2. Thermal resistance between two particles in near contact

The two particles were considered as in near contact only when the gap h_{jk} between the two particles (Fig. 6 (b)) was smaller than $0.5 R_{jk}$ according to the calibration for sphere packings in [42]. Then, similar to the computation of effective thermal resistance between two particles in contact, two particle resistors and one near-contact resistor with a resistance of $R_{jk_{gap}}^{contact}$ were connected in series (Fig. 6 (b)) to compute the effective thermal resistance between two particles in near contact using Eqs. (11)–(13).

$$R_{jk}^{eff} = R_j^P + R_{jk_{gap}}^{contact} + R_k^P \tag{11}$$

$$R_{jk_{gap}}^{contact} = \begin{cases} \left(\pi \cdot \lambda_v \cdot r_{jk} \cdot ln\left(\alpha^2\right)\right)^{-1} \text{ if } \kappa_{jk} \ll 1 \\ \left(\pi \cdot \lambda_v \cdot r_{jk} \cdot ln\left(1 + \chi^2 \cdot R_{jk}\right)\right)^{-1} \text{ otherwise} \end{cases} \tag{12}$$

where κ_{jk} is a sphere separation parameter and defined as:

$$\kappa_{jk} = \frac{\alpha^2 \cdot h_{jk}}{r_{jk}} \tag{13}$$

4. Computation of anisotropic thermal conductivity

For each numerical experiment, the λ_{eff} of the sample under different stress or strain was computed using a thermal network model (TNM)
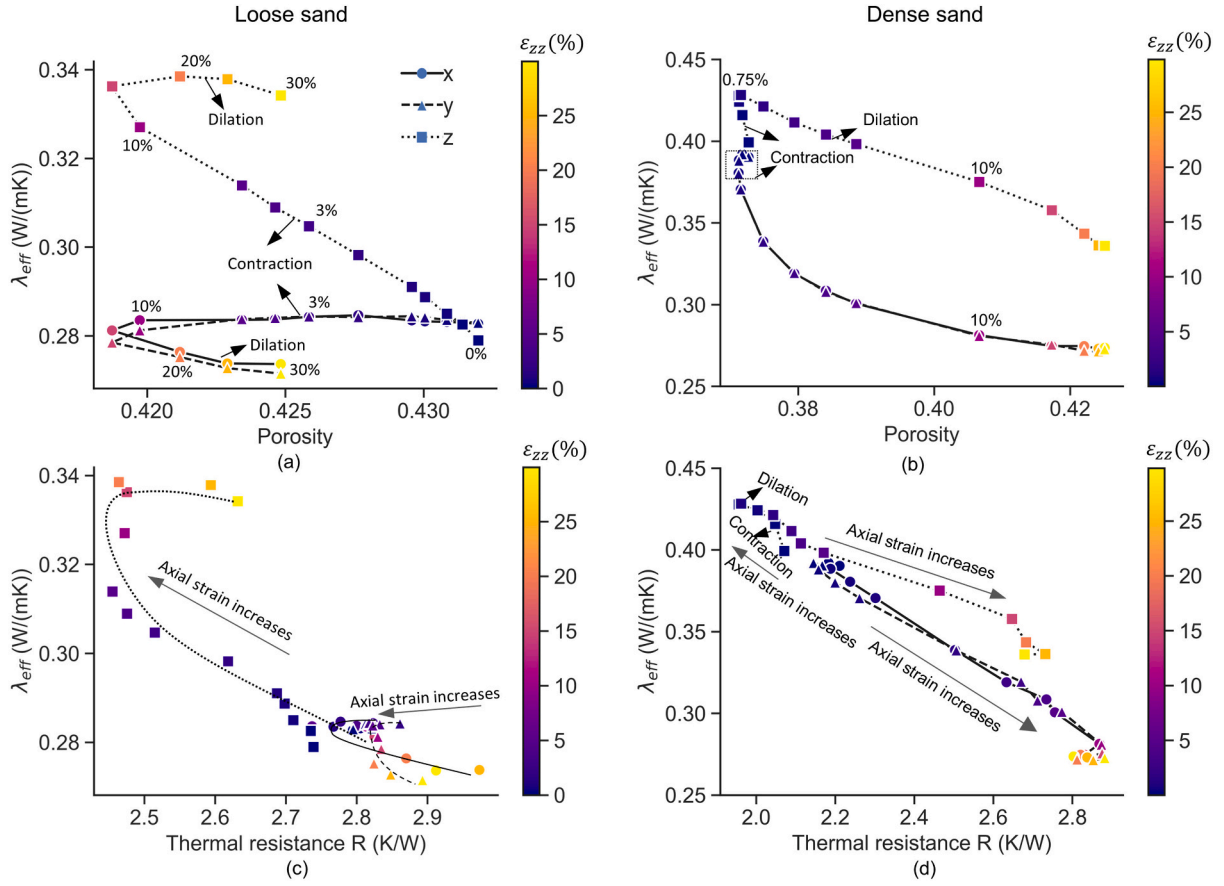
Fig. 12. The evolution of λ_{eff} versus porosity and thermal resistance in triaxial axial compression (i.e. TAC) tests.

based on an undirected weighted thermal network. Eqs. (5) and (8) were used to compute the effective thermal resistance R_{ij}^{eff} for each edge in the thermal network. Then the Eq. (3) can be expressed in a matrix form as:

$$\begin{bmatrix} \frac{1}{R_{ij}^{eff}} & -\frac{1}{R_{ij}^{eff}} \\ -\frac{1}{R_{ij}^{eff}} & \frac{1}{R_{ij}^{eff}} \end{bmatrix} \begin{bmatrix} T_i \\ T_j \end{bmatrix} = \begin{bmatrix} Q_{ij} \\ Q_{ji} \end{bmatrix} \tag{14}$$

By assembling the local matrices into a global matrix as Eq. (15) and knowing the prescribed boundary temperature T_{inlet} and T_{outlet}, the temperature for each particle (T_i and T_j in Eq. (14)) and the heat flux at each network edge (Q_{ij} in Eq. (14)) could be computed. At last, substituting the Q_{ij} and the values of other related parameters to Eq. (16), the λ_{eff} of the sample could be solved.

$$RT = Q \tag{15}$$

$$\lambda_{eff} = \frac{\frac{1}{A}\sum Q_{ij}}{(T_{inlet} - T_{outlet})/L} \tag{16}$$

where A is the area of a cross-section that is perpendicular to the prescribed temperature gradient, and L is the sample length parallel to the prescribed temperature gradient. For each sample in this work, T_{inlet} of 293 K and T_{outlet} computed using a temperature gradient of 400 K/m [42] were assigned to the paired boundaries in x, y and z-direction to compute the λ_{eff} along the three directions. The temperature distributions of the dense sample at 10% axial strain in TAC are shown in Fig. 7, with heat transfers in x, y and z directions.

5. Results and discussions

5.1. Model verification

For the samples under nine levels of isotropic compressions, their λ_{eff} were calculated using TNM when assigning temperature gradient along the z-direction. The results were plotted in Fig. 8 with the λ_{eff} calculated from theoretical models listed in Table 2. The sphere size distribution in the sample is similar to that in Ottawa sand 20–30 [47], so the experimental λ_{eff} of Ottawa sand conducted by Narsilio et al. (2010) [48] was also included in Fig. 8 for comparison. It can be seen that results from the TNM align with experimental results well, and all the data points approximately average all theoretical results, near the Geometric mean (GM). Therefore, the TNM is reliable for calculating λ_{eff} of dry spherical granular materials.

5.2. Relationship between directed network thermal resistance R and λ_{eff}

For each sample at each stress or deformation stage in all the numerical experiments described in Section 2, the porosity, directional λ_{eff} and R in x, y and z directions were calculated and presented in Fig. 9. The porosity only has a linear relationship with λ_{eff} in isotropic and K_0 compression experiments, as shown in Fig. 9 (a). In contrast, Fig. 9 (b) presents that directed network thermal resistance R shows a good linear correlation with λ_{eff} considering all data from all experiments with distinct stress paths. Since R involves particle connectivity, contact quality and contact orientation, the evolution of R and the contact attributes in different numerical experiments will be discussed in the following sections.
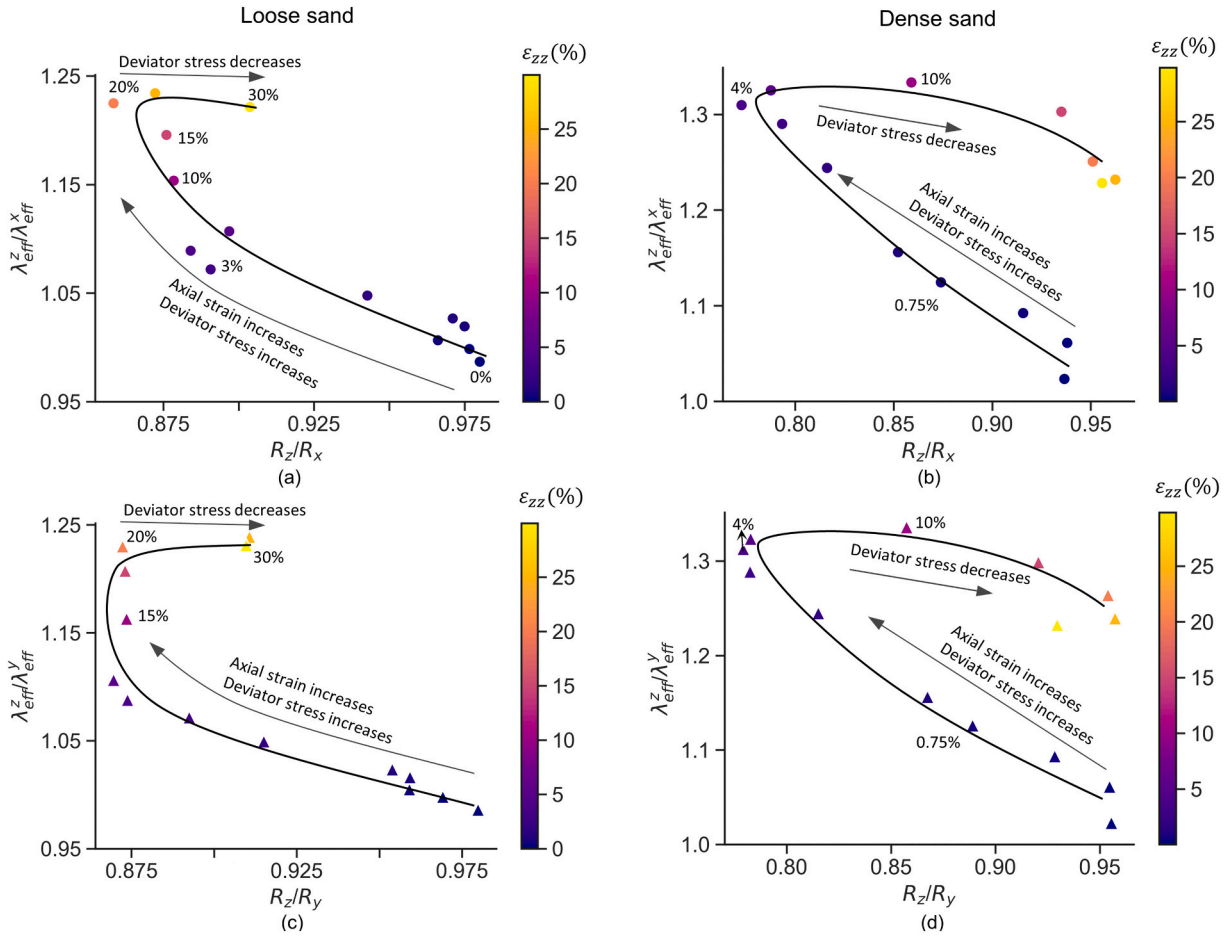
Fig. 13. The ratio of directed network thermal resistance versus thermal anisotropy in TAC tests of loose sand (left column) and dense sand (right column).

5.3. Evolution of thermal anisotropy under isotropic and K_0 compression

Temperature gradients were applied along x and y directions to the sample in the isotropic compression test. Fig. 10 (a) presents that the λ_{eff} calculated from TNM increases with the increase of compressive stress. The λ_{eff} in different directions are the same, indicating the reliability of the thermal network model. The λ_{eff} decreases with the increase of thermal resistance R, indicating that thermal resistance could be the alternative of stress as a parameter for λ_{eff} prediction.

The sample-scale thermal resistance R in this paper is a structural parameter including information about particle connectivity, heat transfer capacity (i.e., thermal resistance) at local interparticle contacts and near-contacts, and the contact orientations. Hence, the distribution of contact orientation and thermal resistance were plotted in Appendix A. If the contact orientation is parallel to the prescribed boundary temperature gradient, the angle of contact orientation (θ in Fig. 5) is 0°. In contrast, θ is 90° when the contact orientation is perpendicular to the temperature gradient and no heat transfer through the contact. The first and fourth rows in Appendix A exhibit that the interparticle contacts (red areas) expand while the near contacts (blue areas) shrink with the increase of compressive stress, indicating that larger compressive stress transforms near-contacts to interparticle contacts with a similar extent in both x and z directions. Additionally, the increasing amount of interparticle contacts indicates that particles moved closer to each other, so the thermal resistances at the interparticle contacts become smaller as shown in the second and fifth rows. Although particles moving closer can also generate new near-contacts, their thermal resistances were high, as shown in the third and sixth rows.

As for the sample under K_0 loading, the larger stress along z-direction results in a larger λ_{eff} than in x and y directions, as shown in Fig. 10 (b). The main reason accounting for the thermal anisotropy is the change of contact orientation according to the distribution of contact orientation and thermal resistance in Appendix B. With the increase of stress, more interparticle contacts were formed with a smaller inclined angle to the z-axis than those in the x-axis. Specifically, while more interparticle contacts orientate around 60° away from the x-direction, the angles to z-direction are smaller and a peak appears around 40° when the axial stress is 1500 kPa. The variation of thermal resistance at interparticle contacts in x and z directions have the almost same decreasing pattern with the increase of axial stress. The variations of thermal resistance at near-contacts in x and z directions are also similar, with near-contacts at 0° in z-direction having slightly larger thermal resistance than those in the x-direction under high compressive stress.

5.4. Evolution of thermal anisotropy in triaxial axial compression (TAC)

The boundaries of the samples in isotropic and K_0 compression tests are moved by increasing compressive stresses. In contrast, the sample deformation in a triaxial test is induced by the boundary displacement in one direction while keeping the stresses on other boundaries unchanged, which is also referred to as shear-induced deformation. In this section, z-direction displacement (contraction) was assigned to both loose and dense sand samples to investigate the applicability of the new sample-scale thermal resistance R and the effect of dilatancy on anisotropic λ_{eff}.

Fig. 11 (a) presents that the deviator stress of dense sand reaches the peak at a small axial strain of 2%, and it meets the deviator stress of loose sand at the axial strain of 18%. The dense sand contracts from the beginning and turns into dilation when the axial strain is around 0.75, as
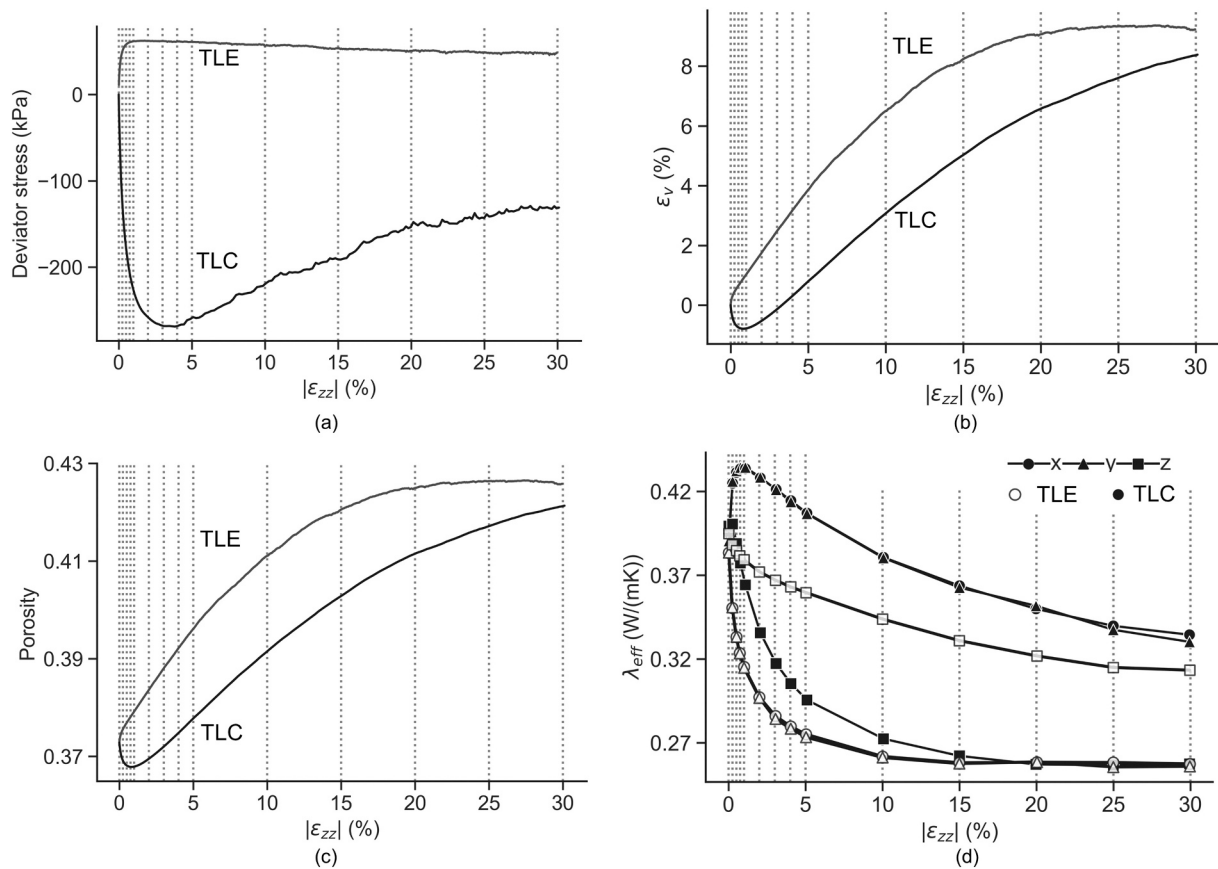
Fig. 14. The evolution of stress (a), volume strain (b), porosity (c) and λ_{eff} (d) in triaxial lateral extension (i.e., TLE) and compression (i.e., TLC) tests.

observed in the evolution of volume strain (Fig. 11 (b)) and porosity Fig. 11 (c). The dilatancy happens earlier than the peak of deviator stress in dense sand, while the effective thermal conductivity in the z-direction λ_{eff}^z reaches its peak at the same time as shown in Fig. 11 (d). In addition, the porosity of dense sand and loose sand also meet earlier than their deviator stress. Therefore, the non-synchronous stress with the variation of microstructure implies that including stress in a model to study the λ_{eff} evolution may be inaccurate. The loose sand also presents a slight dilation when the ε_{zz} is larger than 15%, which may be because of the sample is a hexahedron with rigid walls rather than a cylinder with a soft membrane in the laboratory test.

The evolution of λ_{eff} varies in different directions due to the stress-induced sample anisotropy. The effective thermal conductivity in x and y-direction $\lambda_{eff}^{x/y}$ also experience an increase in the beginning but the peak is smaller and happens earlier than λ_{eff}^z. In addition, the λ_{eff}^z of dense and loose sand meet when the strain ε_{zz} is larger than 20%. In contrast, $\lambda_{eff}^{x/y}$ of the two sands reach a similar steady value at a much earlier stage with ε_{zz} of 10%.

The larger λ_{eff}^z than $\lambda_{eff}^{x/y}$ is mainly because the interparticle contacts are prone to orientate to the contraction direction (i.e., z-direction) according to the contact orientation and thermal resistance distribution of loose sand in Appendix C and dense sand in Appendix D. The interparticle contact (red areas) in the first row of Appendix C remain similarly with the strain ε_{zz} increases, especially when ε_{zz} is larger than 10%. In contrast, the shape of interparticle contact effect (red area) in the fourth row experiences a distinguishable change, with more real contacts (red bars) pointing at 50° that pointing at 90° at the end of the experiment. These new contacts with a small orientation angle to z-direction (i.e., the contractional direction in TAC) can shorten the z-directional preferential heat transfer paths and result in a high λ_{eff}^z. Similarly, more interparticle contacts also have smaller inclination angle with z direction in TAC for the dense sand comparing the first and fourth

rows in Appendix D.

Since the peak of $\lambda_{eff}^{x/y}$ and λ_{eff}^z of the dense sand do not happen at the same moment in Fig. 11 (d), the contribution of contact attributes to them are investigated. While interparticle contacts (red areas) in the first two rows of Appendix D have little change before ε_{zz} reaches 0.75%, the near contacts (blue bars) with inclination angle smaller than 30° become shorter at ε_{zz} of 0.75% and then longer in the third row. The smaller thermal resistance of near-contacts leads to the early peak of $\lambda_{eff}^{x/y}$. In contrast, the near contact (blue) bars between 0° and 30° in the last row of Appendix D become longer when ε_{zz} is 0.75%. The decrease of λ_{eff}^z after the peak is because of the change of interparticle contact orientation, since the main axis of the real contact (red) shape in the fourth row rotates from 50° to almost 60° while their thermal resistances remain the same when ε_{zz} increases from 4.9% to 29.81%.

Fig. 12 (a) and (b) show that the relationship between porosity and λ_{eff} is clearly divided into two groups related to z and x/y directions. In contrast, the relationship between R and λ_{eff} can match a relatively uniform curve, as shown in Fig. 12 (c) and (d). If observing the evolution of R locally, R can also indicate the sample volume deformation. For example, the R in the z-direction of the loose sand in Fig. 12 (c) has a turning point at ε_{zz} of 15% where the sample deformation changes from contraction to dilatancy. The R in the z-direction of dense sand also reaches its lowest value at ε_{zz} of 0.75% in Fig. 12 (d) when the sample starts to dilate.

By applying the ratio of z-directional λ_{eff}^z to the x or y directional λ_{eff}, two parameters $\lambda_{eff}^z/\lambda_{eff}^x$ and $\lambda_{eff}^z/\lambda_{eff}^y$ are used as indicators of thermal anisotropy. A ratio of λ_{eff} of 1 means thermal isotropy while a value deviating from 1 means thermal anisotropy becomes higher. Likewise, R_z/R_x and R_z/R_y are used to explore their relationship with thermal anisotropy.

Fig. 13 shows that R_z/R_x and R_z/R_y can capture the stress-induced thermal anisotropy evolution. The thermal anisotropy becomes higher
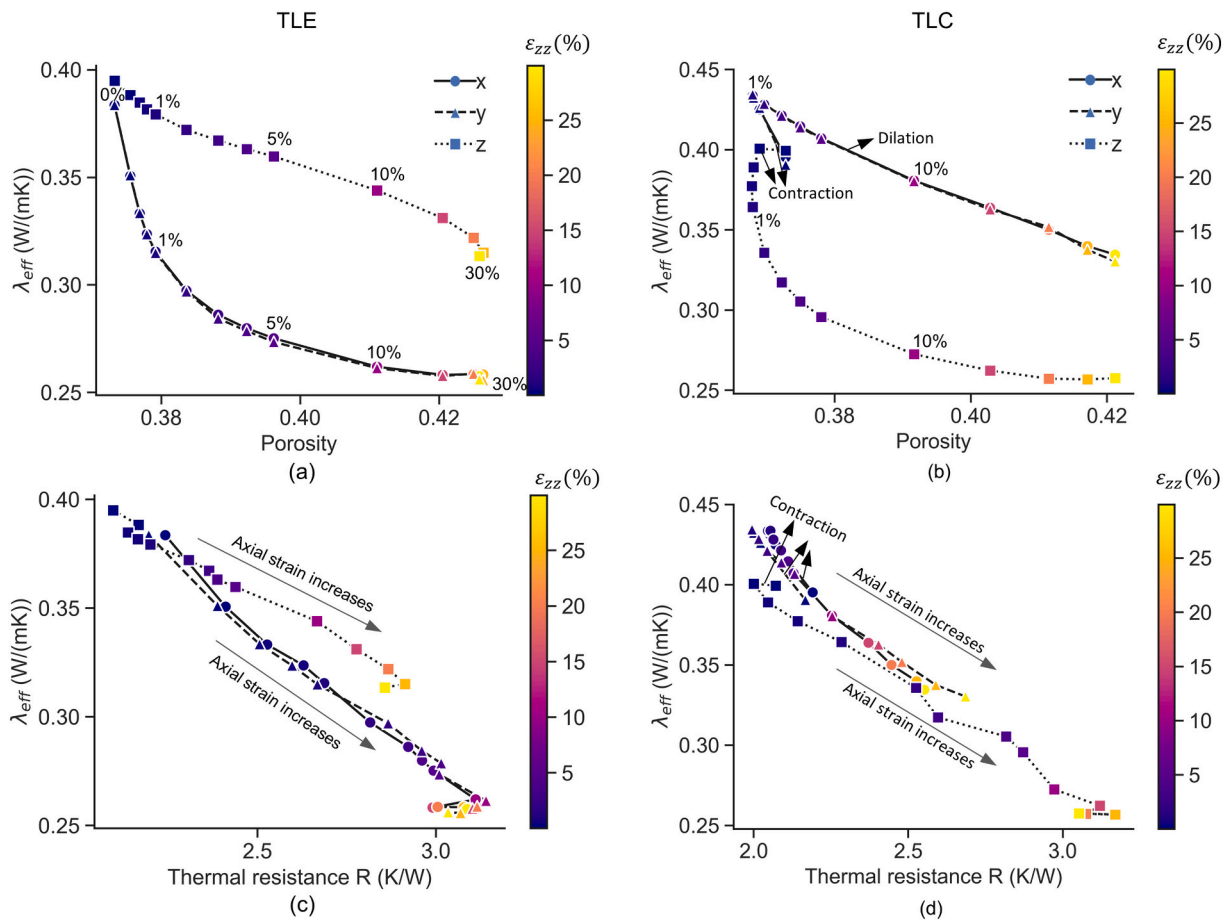
Fig. 15. The evolution of λ_{eff} versus porosity and thermal resistance in triaxial lateral extension (left column) and compression tests (right column).

as the ratio of R decreases and later become lighter as the ratio of R increases after axial strain reaches 20% and 4% in loose sand and dense sand, respectively. The turning point appears at a similar moment to the appearance of the turning point shown in the evolution of deviator stress in Fig. 11(a), but is later than the turning point shown in the evolution of sample volume in Fig. 11(b).

5.5. Evolution of thermal anisotropy in triaxial lateral extension (TLE) and compression (TLC)

The dense sand sample in the TAC test was also used to simulate a TLE test corresponding to the active retaining wall and a TLC test corresponding to the passive retaining wall. As shown in Fig. 1, σ'_1 is constant while horizontal σ'_3 decreases in TLE, so the sample in TLE still contracts in the z-direction and dilates in the x/y direction. Fig. 14(a) shows that the deviator stress in TLE increases and reach a steady-state in a short period. In contrast, σ'_1 is constant while σ'_3 increases in TLC, resulting in a negative deviator stress and dilation in z-direction while a contraction in x/y direction. The negative deviator stress reaches its bottom at the strain of around 3.5%. The change of volume strain and porosity in Fig. 14(b) and (c) exhibit that the sample in TLE keeps dilating in the whole period of the experiment while the sample in TLC contracts in the begging and then dilates when the stain is larger than 0.75. Similar to the observation in the TAC experiment presenting the stress status in shallow foundations, the dilation in TLC also happens before the turning point of deviator stress.

In TLE, λ_{eff} in all directions have downward trends, with a larger value in the z-direction than that in the x/y direction, as shown in Fig. 14 (d). According to the contact orientation and thermal resistance distribution in Appendix E, the amount of interparticle contacts with a small

inclination to z-direction shown in the fourth row is larger than that to x and y directions shown in the first row, leading to the larger λ_{eff}^z than $\lambda_{eff}^{x/y}$. This observation is consistent in the previous K_0 and TAC tests. However, the reason accoutring for the evolutions of λ_{eff}^z and $\lambda_{eff}^{x/y}$ are different. The real contact (red) bars in the first row become shorter while near contacts (blue) bars become longer when contact orientation is between 30° and 60° shown in the first row, indicating that the decrease of $\lambda_{eff}^{x/y}$ is mainly because the interparticle contacts in dilational direction turn into near-contacts when the stress decreases. In contrast, the decrease in the number of interparticle contacts only accounts for the decline of λ_{eff}^z before strain is 5%. After that, the decrease of λ_{eff}^z is mainly because the interparticle contacts incline away from the prescribed temperature gradient, which could be observed in the fourth row where the main axis of the red area rotates from 45° to 60°.

The λ_{eff}^z is always smaller than $\lambda_{eff}^{x/y}$ (Fig. 14(d)) in TLC because the sample dilates in z-direction while contracting in x and y directions. It is also because more interparticle contacts have a smaller inclination angle to the contractional direction (x/y direction) than that to the dilational direction (z-direction), by comparing the first and fourth row in Appendix F. Similar to TAC of the dense sand, the peak of effective thermal conductivity in the dilational direction (λ_{eff}^z) happens earlier than that of contractional direction ($\lambda_{eff}^{x/y}$) in Fig. 14(d), and similar evolution of contact attributes are observed in Appendix F. The peak of λ_{eff}^z is because z-directional thermal resistances of near-contacts below 30° are smallest at strain of 1.09% during TLC test, while the increased amount of interparticle contacts orientating 30° to 50° contribute to the peak of $\lambda_{eff}^{x/y}$.

The analysis of microstructure to λ_{eff} reveals that the particle connectivity (i.e., amount of contacts), contact quality (i.e., thermal resistance) and contact orientation together contribute to the λ_{eff}. The new
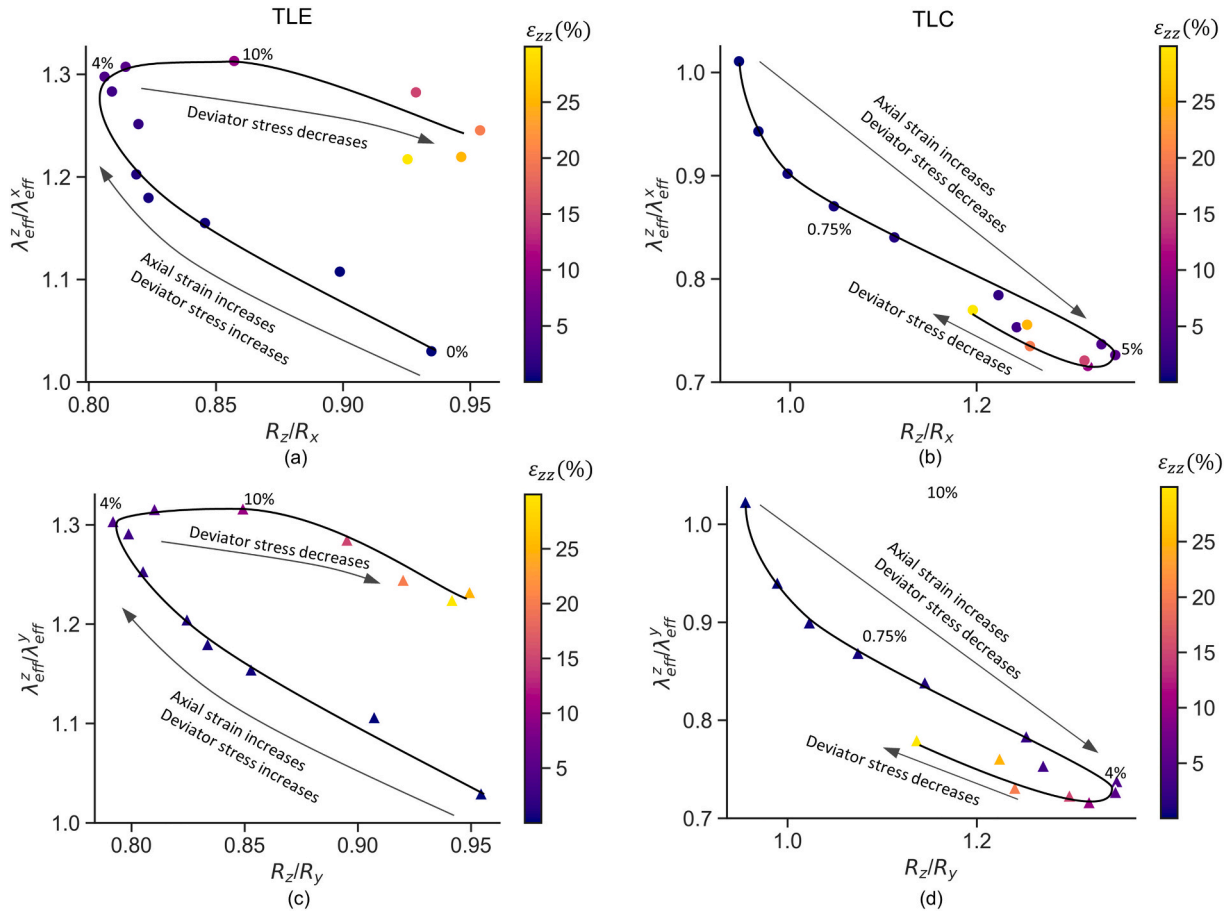
Fig. 16. The ratio of directed network thermal resistance versus thermal anisotropy in the TLE test (left column) and TLC test (right column).

developed directed network thermal resistance R has involved the three factors and their relationship with λ_{eff} of deforming samples in TLE and TLC tests are shown in Fig. 15. While two groups still exist in the relationship between porosity and λ_{eff} related to different directions, the correlation between R and anisotropic λ_{eff} shows a general linear downward trend. In addition, the smallest R in Fig. 15 (d) is still related to the moment when the sample turns from contraction to dilation in TLC.

Fig. 16 shows that R_z/R_x and R_z/R_y can also capture the stress-induced thermal anisotropy evolution in TLE and TLC. In TLE, thermal anisotropy indicated by $\lambda_{eff}^z/\lambda_{eff}^{x/y}$ becomes higher as the ratio of R decreases at an early deformation stage when axial strain is smaller than 4%. After that, thermal anisotropy experiences a slight decline while the ratio of R increases. Similar to the observation in the triaxial axial compression test, the turning point in TLE is also because of the deviator stress change (Fig. 15(a)). Since the λ_{eff}^z in TLC is smaller than $\lambda_{eff}^{x/y}$, thermal anisotropy become higher when $\lambda_{eff}^z/\lambda_{eff}^{x/y}$ decreases until the strain rate reaches 5%. The turning point of thermal anisotropy in TLC is also because of deviator stress change and the strain rate corresponding to the turning point is similar to that in TLE.

6. Conclusion

To bridge the research gap that rare microstructural parameters can be used to investigate stress-induced thermal anisotropy, this paper introduced a directed thermal network and generated a new *directed network thermal resistance R* based on the geometrical information from the network. The evolution of effective thermal conductivity λ_{eff} in three

Orthogonal directions, porosity and contact attributes were investigated in several DEM numerical experiments. Even though stress changes the boundary condition of a sample and its interior structure, its variation does not always synchronize with the evolution of λ_{eff}, but seems to reach a common terminal value at large strains. Hence, involving the stress or deformation modulus in λ_{eff} could also introduce inaccuracy. Furthermore, thermal anisotropy is not only related to the value of λ_{eff} in different directions, but also the evolution difference. In experiments such as TAC and TLC for dense sand, the peak of λ_{eff} in dilational direction happens earlier than that in contractional direction. Stress-related parameters also cannot characterise this evolution difference, so new directed microstructural parameters are required.

Since interparticle contacts and near-contacts play key roles in heat transfer paths in dry granular materials, the effects of three contact attributes: connectivity, quality and orientation on anisotropic λ_{eff} evolution was investigated. Results show that the usually ignored interparticle contact orientation controls the anisotropic λ_{eff} as interparticle contacts orientate more to the sample contractional direction than the dilational direction. In TAC and TLC tests, the reasons accounting for the λ_{eff} peaks in sample contractional and dilational directions are also different. While the number of interparticle contacts plays the dominative role before the λ_{eff} peak in the contractional direction, the thermal resistance of near-contacts controls the λ_{eff} peak in the dilational direction.

The calculation of *network thermal resistance R* considers the contribution of particle connectivity, quality and orientation. Therefore, R shows the advantage of presenting an inversely proportional relationship with anisotropic λ_{eff} regardless of the heat transfer direction, and the ratio of R can capture the evolution of stress-induced thermal
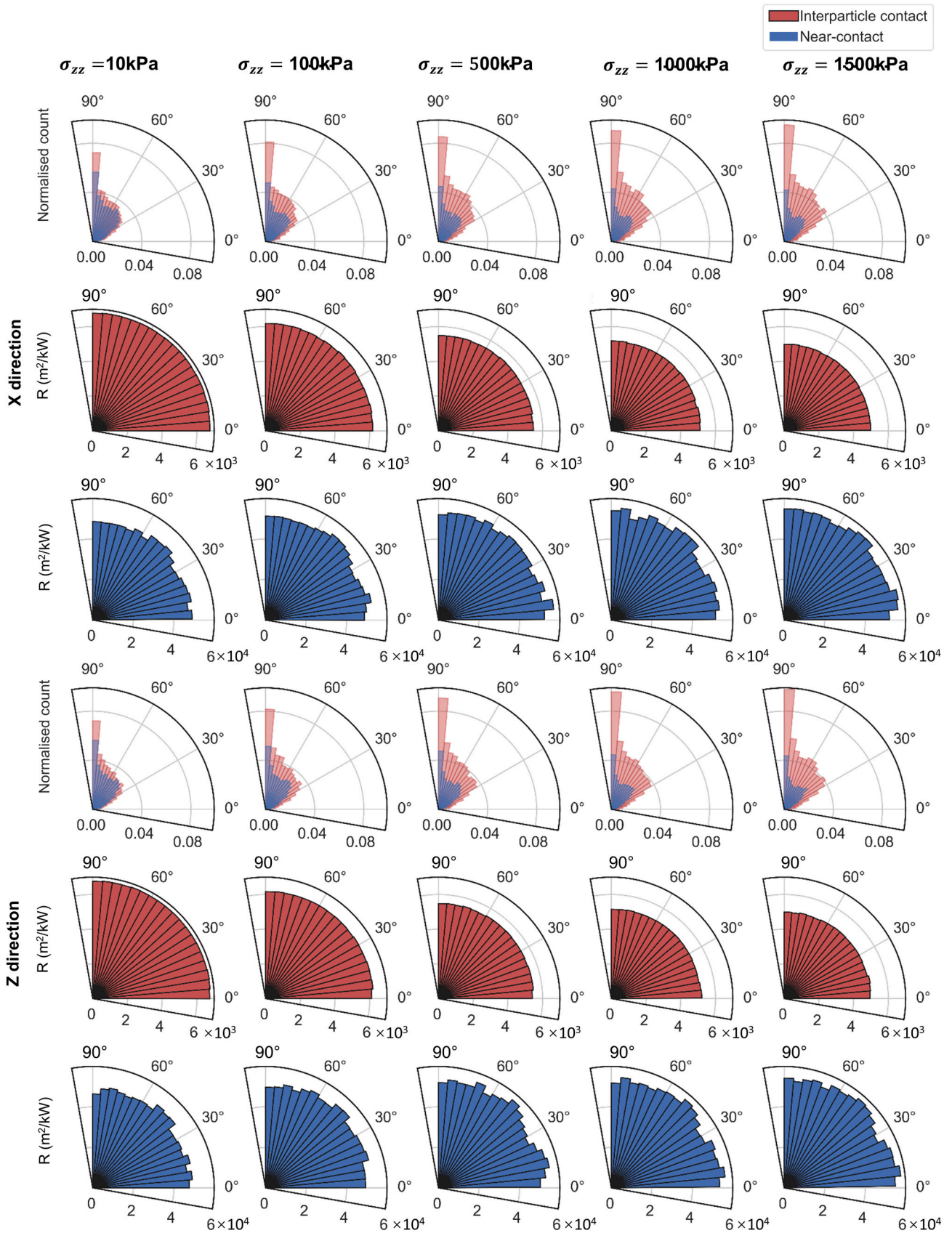
Appendix A. Contact orientation and thermal resistance distribution under isotropic compression.
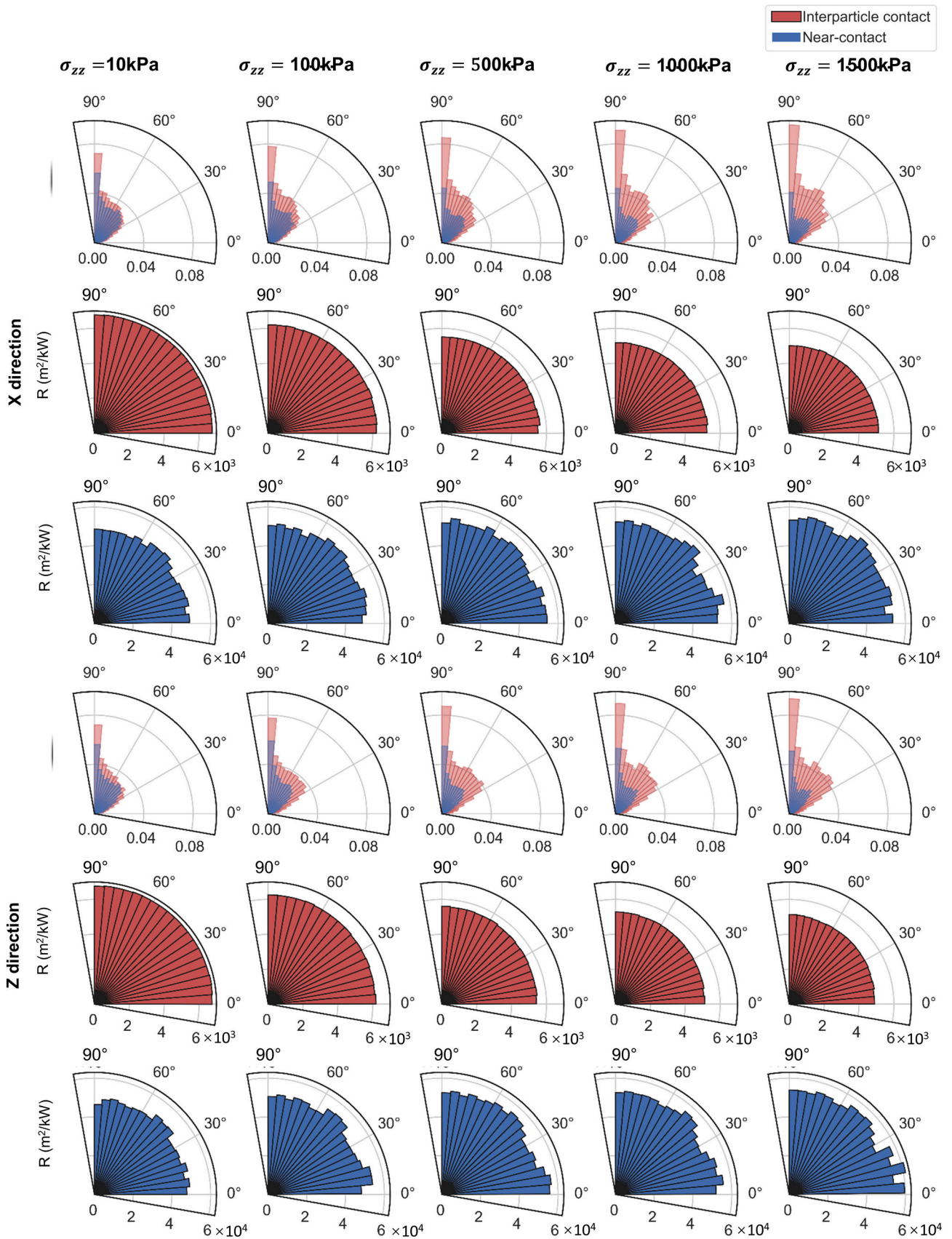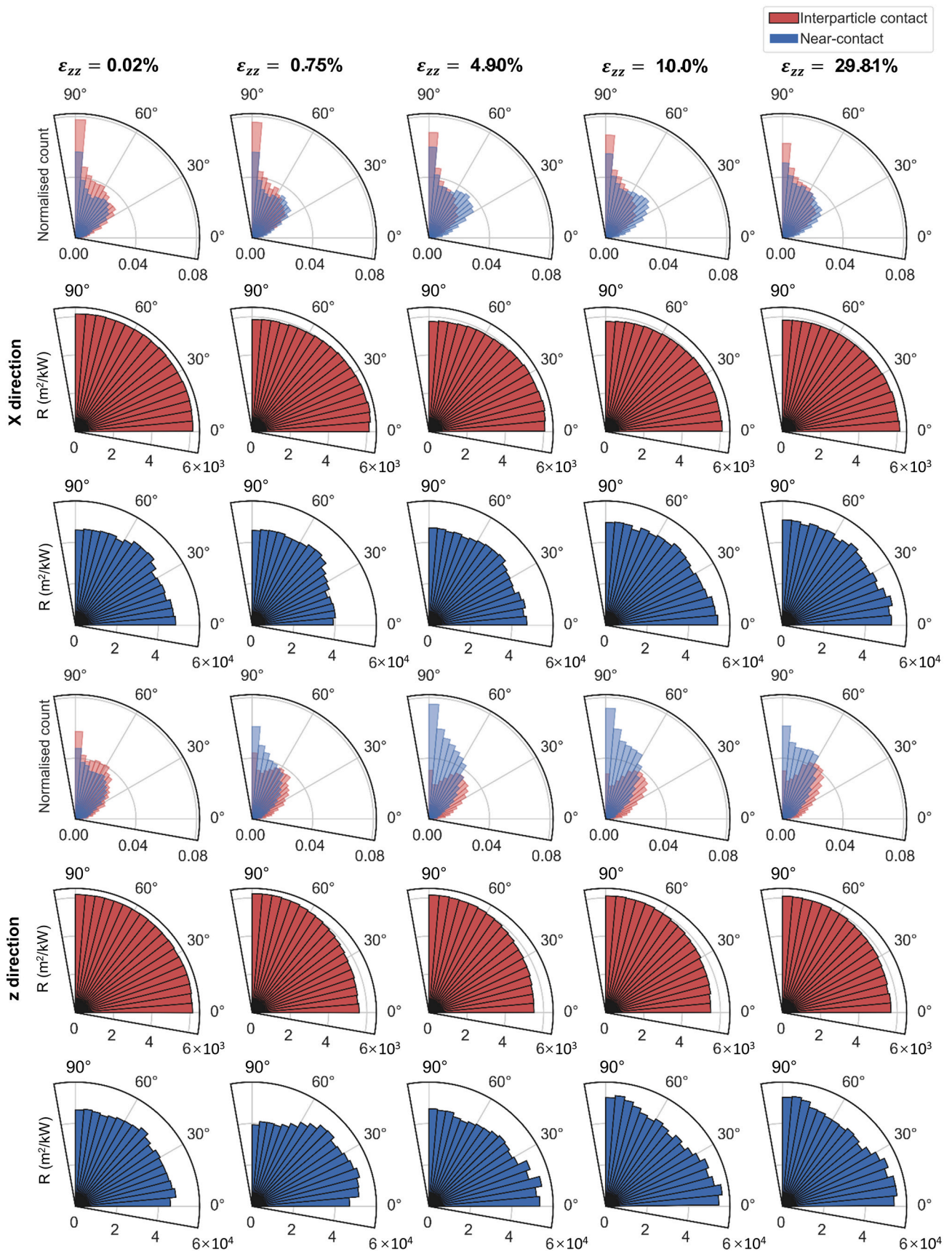
Appendix B. Contact orientation and thermal resistance distribution under K0 compression.
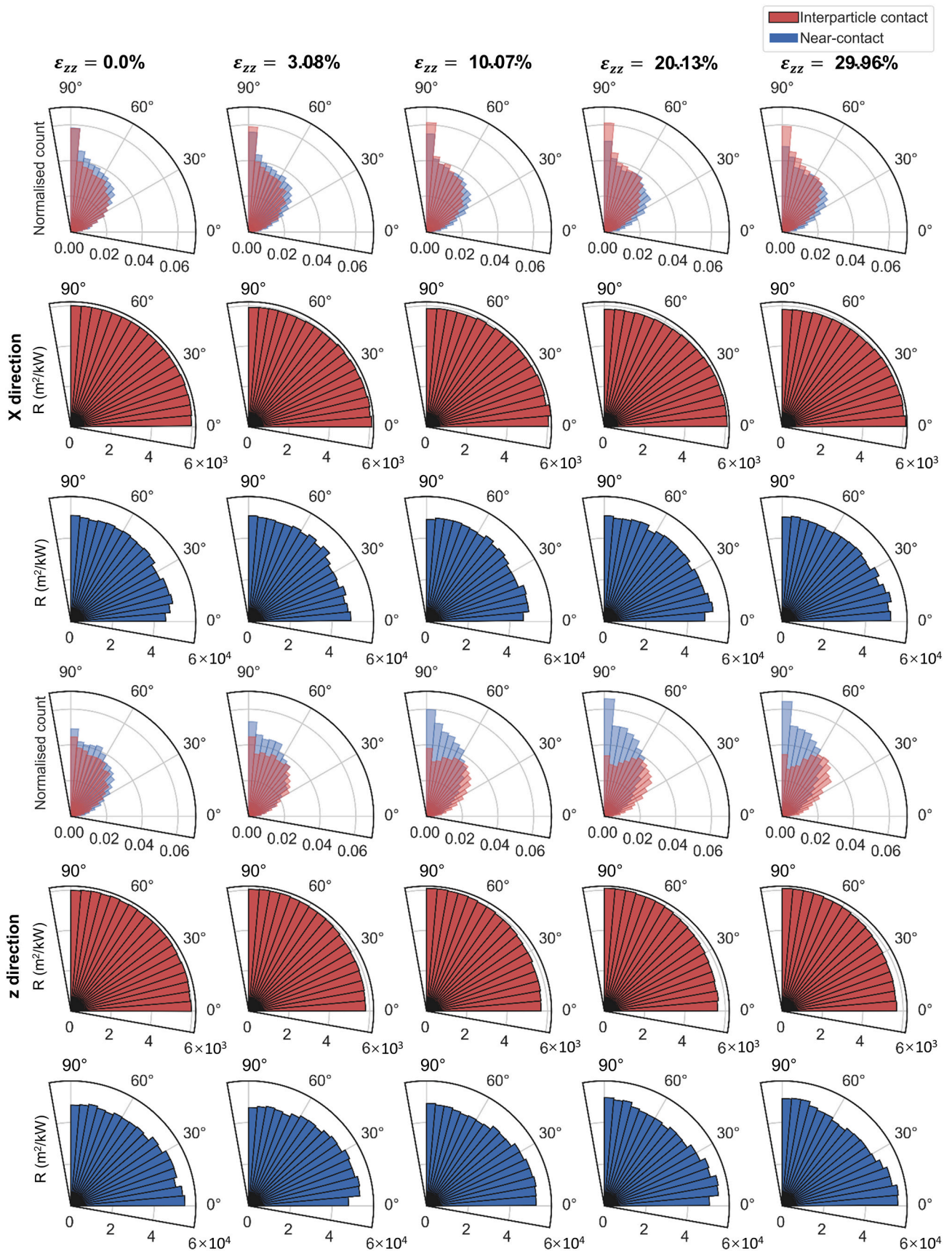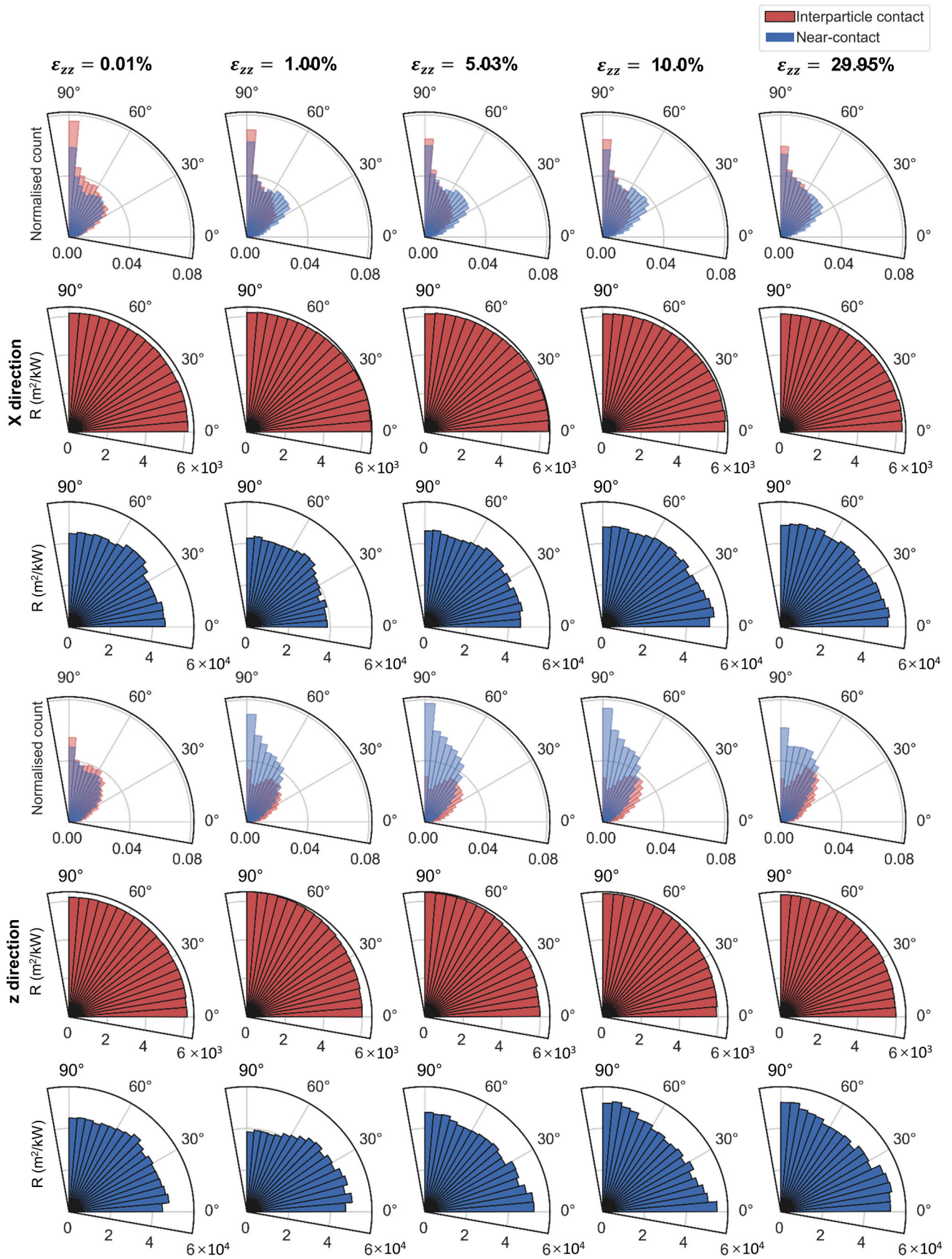
Appendix C. Contact orientation and thermal resistance distribution under triaxial axial compression for loose sand.
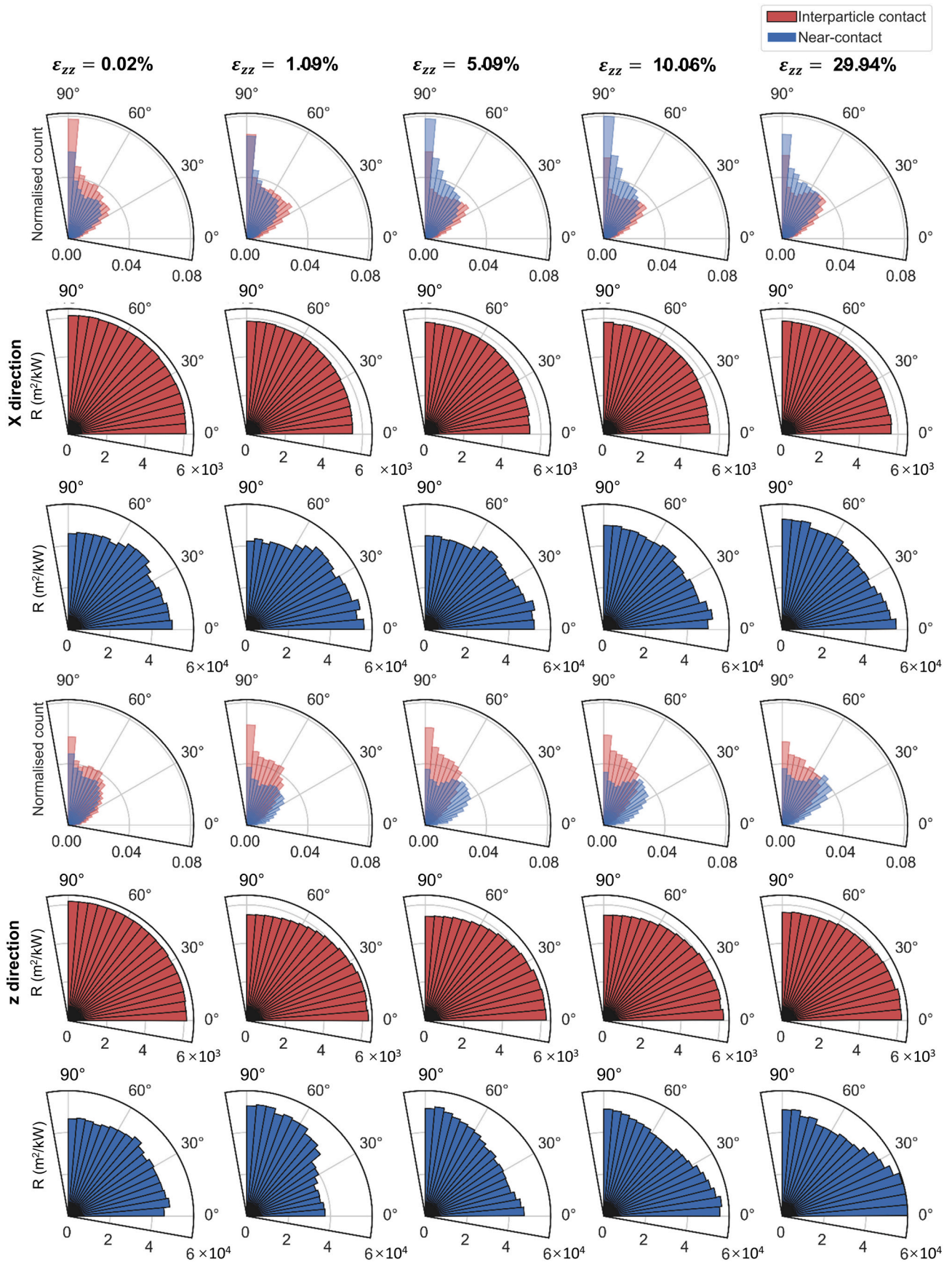
Appendix D. Contact orientation and thermal resistance distribution under triaxial axial compression for dense sand.

Appendix E. Contact orientation and thermal resistance distribution under triaxial lateral extension for dense sand.

Appendix F. Contact orientation and thermal resistance distribution under triaxial lateral compression for dense sand.

anisotropy. It also emphasises the importance of considering mesoscale structural parameters when analysing the heat transfer and building λ_{eff} models for granular materials. Since the R is based on geometric information, it can also guide the material design when directed λ_{eff} is expected to be enhanced by tunning contacts.

Declaration of Competing Interest

The authors declared that there is no conflict of interest.

Data availability

Data will be made available on request.

Acknowledgments

References

[1] D. Fjaestad, I. Tomac, Experimental investigation of sand proppant particles flow and transport regimes through narrow slots, Powder Technol. 343 (2019) 495–511.

[2] D. Lyu, C. Lin, L. Ren, C. Dong, J. Song, Residual oil evolution based on displacement characteristic curve, Int. J. Rock Mech. Min. Sci. 30 (2020) 337–343.

[3] W. Zhou, Q. Ma, G. Ma, X. Cao, Y. Cheng, Microscopic investigation of internal erosion in binary mixtures via the coupled LBM-DEM method, Powder Technol. 376 (2020) 31–41.

[4] W.B. Fei, Q. Li, X.C. Wei, R.R. Song, M. Jing, X.C. Li, Interaction analysis for CO2 geological storage and underground coal mining in Ordos Basin, China, Eng. Geol. 196 (2015) 194–209.

[5] Y. Zhong, G.A. Narsilio, N. Makasis, C. Scott, Experimental and numerical studies on an energy piled wall: the effect of thermally activated pile spacing, Geomech. Energy Environ. 29 (2022), 100276.

[6] T. Yun, B. Dumas, J.C. Santamarina, Heat transport in granular materials during cyclic fluid flow, Granul. Matter 13 (2011) 29–37.

[7] W. Fei, G.A. Narsilio, M.M. Disfani, Impact of three-dimensional sphericity and roundness on heat transfer in granular materials, Powder Technol. 355 (2019) 770–781.

[8] G. Wei, H. Zhang, X. An, S. Jiang, Influence of particle shape on microstructure and heat transfer characteristics in blast furnace raceway with CFD-DEM approach, Powder Technol. 361 (2020) 283–296.

[9] L. Wang, X. An, Y. Wu, Q. Qian, R. Zou, K. Dong, DEM simulation of vibrated packing densification of mono-sized regular octahedral particles, Powder Technol. 384 (2021) 29–35.

[10] Z. Abdulagatova, I. Abdulagatov, V. Emirov, Effect of temperature and pressure on the thermal conductivity of sandstone, Int. J. Rock Mech. Min. Sci. 46 (2009) 1055–1071.

[11] G. Cheng, A. Yu, P. Zulli, Evaluation of effective thermal conductivity from the structure of a packed bed, Chem. Eng. Sci. 54 (1999) 4199–4209.

[12] W. Dai, D. Hanaor, Y. Gan, The effects of packing structure on the effective thermal conductivity of granular media: a grain scale investigation, Int. J. Therm. Sci. 142 (2019) 266–279.

[13] W. Siu, S.-K. Lee, Effective conductivity computation of a packed bed using constriction resistance and contact angle effects, Int. J. Heat Mass Transf. 43 (2000) 3917–3924.

[14] G.K. Batchelor, R. O'brien, Thermal or electrical conduction through a granular material, Proc. R. Soc. Lond. A 355 (1977) 313–333.

[15] M. Kaganer, Contact heat transfer in granular material under vacuum, JEP 11 (1966) 19–22.

[16] C. Chan, C. Tien, Conductance of packed spheres in vacuum, 1973.

[17] F. Tehranian, M.A. Abdou, Experimental study of the effect of external pressure on particle bed effective thermal properties, Fusion Technol. 27 (1995) 298–313.

[18] S. Zhao, J. Zhao, Y. Lai, Multiscale modeling of thermo-mechanical responses of granular materials: a hierarchical continuum–discrete coupling approach, Comput. Methods Appl. Mech. Eng. 367 (2020), 113100.

[19] D. Garrett, H. Ban, Compressive pressure dependent anisotropic effective thermal conductivity of granular beds, Granul. Matter 13 (2011) 685.

[20] L. Papadopoulos, M.A. Porter, K.E. Daniels, D.S. Bassett, Network analysis of particles and grains, J. Complex Netw. 6 (2018) 485–565.

[21] J.H. van der Linden, G.A. Narsilio, A. Tordesillas, Machine learning framework for analysis of transport through complex networks in porous, granular media: a focus on permeability, PhRvE 94 (2016), 022904.

[22] O. Birkholz, Y. Gan, M. Kamlah, Modeling the effective conductivity of the solid and the pore phase in granular materials using resistor networks, Powder Technol. 351 (2019) 54–65.

[23] W. Fei, G.A. Narsilio, Network analysis of heat transfer in sands, Comput. Geotech. 127 (2020), 103773.

[24] W. Fei, G.A. Narsilio, J.H. van der Linden, A. Tordesillas, M.M. Disfani, J. C. Santamarina, Impact of particle shape on networks in sands, Comput. Geotech. 137 (2021), 104258.

[25] X.C. Li, X.Y. Huang, Numerical investigation of thermal conductivity of particle dispersive composites based on fractal method, advanced materials research, Trans. Tech. Publ. (2013) 1808–1812.

[26] I.L. Ngo, V.A. Truong, An investigation on effective thermal conductivity of hybrid-filler polymer composites under effects of random particle distribution, particle size and thermal contact resistance, Int. J. Heat Mass Transf. 144 (2019), 118605.

[27] A. Mohamad, Thermal contact theory for estimating the thermal conductivity of nanofluids and composite materials, Appl. Therm. Eng. 120 (2017) 179–186.

[28] A. Tordesillas, S.T. Tobin, M. Cil, K. Alshibli, R.P. Behringer, Network flow model of force transmission in unbonded and bonded granular media, PhRvE 91 (2015), 062204.

[29] A. Tordesillas, D.M. Walker, Q. Lin, Force cycles and force chains, PhRvE 81 (2010), 011302.

[30] J.S. McCartney, M. Sánchez, I. Tomac, Energy geotechnics: advances in subsurface energy recovery, storage, exchange, and waste management, Comput. Geotech. 75 (2016) 244–256.

[31] F. Torresan, L. Piccinini, M. Pola, D. Zampieri, P. Fabbri, 3D hydrogeological reconstruction of the fault-controlled Euganean geothermal system (NE Italy), Eng. Geol. 274 (2020).

[32] A. Bidarmaghz, N. Makasis, W. Fei, G.A. Narsilio, An efficient and sustainable approach for cooling underground substations, Tunnel. Underground Space Technol. 113 (2021), 103986.

[33] C. Kloss, C. Goniva, A. Hager, S. Amberger, S. Pirker, Models, algorithms and validation for opensource DEM and CFD–DEM, Progr. Comp. Fluid Dynam. Int. J. 12 (2012) 140–152.

[34] R. Holtzman, D.B. Silin, T.W. Patzek, Frictional granular mechanics: a variational approach, IJNME 81 (2010) 1259–1280.

[35] S. Yimsiri, K. Soga, Effects of soil fabric on behaviors of granular soils: microscopic modeling, Comput. Geotech. 38 (2011) 861–874.

[36] F. Da Cruz, S. Emam, M. Prochnow, J.-N. Roux, F. Chevoir, Rheophysics of dense granular materials: discrete simulation of plane shear flows, PhRvE 72 (2005), 021309.

[37] J.L. Perez, C. Kwok, X. Huang, K. Hanley, Assessing the quasi-static conditions for shearing in granular media within the critical state soil mechanics framework, Soils Found. 56 (2016) 152–159.

[38] Y. Asakuma, Y. Kanazawa, T. Yamamoto, Thermal radiation analysis of packed bed by a homogenization method, Int. J. Heat Mass Transf. 73 (2014) 97–102.

[39] R. Askari, S.H. Hejazi, M. Sahimi, Thermal conduction in deforming isotropic and anisotropic granular porous media with rough grain surface, TPM 124 (2018) 221–236.

[40] W. Fei, G.A. Narsilio, J.H. van der Linden, M.M. Disfani, Network analysis of heat transfer in sphere packings, Powder Technol. 362 (2020) 790–804.

[41] COMSOL AB, COMSOL Multiphysics v5.0. http://www.comsol.com, 2015.

[42] T.S. Yun, T.M. Evans, Three-dimensional random network model for thermal conductivity in particulate materials, Comput. Geotech. 37 (2010) 991–998.

[43] T.S. Yun, J.C. Santamarina, Fundamental study of thermal conduction in dry soils, Granul. Matter 10 (2008) 197–207.

[44] R. Penide-Fernandez, F. Sansoz, Microscale Knudsen effect over the transverse thermal conductivity of woven ceramic fabrics under compression, Int. J. Heat Mass Transf. 171 (2021), 121085.

[45] Z. Guo, J. Yang, S. Zhang, Z. Tan, X. Tian, Q. Wang, Numerical calibration for thermal resistance in discrete element method by finite volume method, Powder Technol. 383 (2021) 584–597.

[46] S. Suo, M. Moscardini, V. Becker, Y. Gan, M. Kamlah, Cyclic thermo-mechanical performance of granular beds: effect of elastoplasticity, Powder Technol. 394 (2021) 705–713.

[47] V. Marzulli, C.S. Sandeep, K. Senetakis, F. Cafaro, T. Pöschel, Scale and water effects on the friction angles of two granular soils with different roughness, Powder Technol. 377 (2021) 813–826.

[48] G.A. Narsilio, J. Kress, T.S. Yun, Characterisation of conduction phenomena in soils at the particle-scale: finite element analyses in conjunction with synthetic 3D imaging, Comput. Geotech. 37 (2010) 828–836.

[49] A.L. DeVera Jr., W. Strieder, Upper and lower bounds on the thermal conductivity of a random, two-phase material, J. Phys. Chem. 81 (1977) 1783–1790.

[50] J. Sass, A.H. Lachenbruch, R.J. Munroe, Thermal conductivity of rocks from measurements on fragments and its application to heat-flow determinations, J. Geophys. Res. 76 (1971) 3391–3401.

[51] Z. Hashin, S. Shtrikman, A variational approach to the theory of the effective magnetic permeability of multiphase materials, J. Appl. Phys. 33 (1962) 3125–3131.

[52] R. Hill, A self-consistent mechanics of composite materials, J. Mech. Phys. Solids 13 (1965) 213–222.

[53] V. Tarnawski, W. Leong, F. Gori, G. Buchan, J. Sundberg, Inter-particle contact heat transfer in soil systems at moderate temperatures, IJER 26 (2002) 1345–1358.